



HAL
open science

Monthly estimation of the surface water extent in France at a 10-m resolution using Sentinel-2 data

Xiucheng Yang, Qiming Qin, Hervé Yésou, Thomas Ledauphin, Mathieu Koehl, P. Grussenmeyer, Zhe Zhu

► **To cite this version:**

Xiucheng Yang, Qiming Qin, Hervé Yésou, Thomas Ledauphin, Mathieu Koehl, et al.. Monthly estimation of the surface water extent in France at a 10-m resolution using Sentinel-2 data. Remote Sensing of Environment, 2020, 244, pp.111803 -. 10.1016/j.rse.2020.111803 . hal-03490249

HAL Id: hal-03490249

<https://hal.science/hal-03490249>

Submitted on 20 May 2022

HAL is a multi-disciplinary open access archive for the deposit and dissemination of scientific research documents, whether they are published or not. The documents may come from teaching and research institutions in France or abroad, or from public or private research centers.

L'archive ouverte pluridisciplinaire **HAL**, est destinée au dépôt et à la diffusion de documents scientifiques de niveau recherche, publiés ou non, émanant des établissements d'enseignement et de recherche français ou étrangers, des laboratoires publics ou privés.



Distributed under a Creative Commons Attribution - NonCommercial 4.0 International License

1 Monthly estimation of the surface water extent in France at a 10-m resolution 2 using Sentinel-2 data

3 Xiucheng Yang^{1,2*}, Qiming Qin^{1,3}, Hervé Yésou⁴, Thomas Ledauphin⁴, Mathieu Koehl², Pierre Grussenmeyer², Zhe Zhu⁵

4 ¹ Institute of Remote Sensing and Geographic Information System, Peking University, 100871, Beijing, China

5 ² Photogrammetry and Geomatics Group, ICube UMR 7357, INSA Strasbourg, University of Strasbourg, 67084, Strasbourg, France

6 ³ Geographic information system technology innovation center of the Ministry of natural resources of China, Beijing, China

7 ⁴ ICube-SERTIT, UMR 7357, Institut Telecom Physiques Strasbourg, University of Strasbourg,

8 67412 Illkirch Graffenstaden, France

9 ⁵ Department of Natural Resources and the Environment, University of Connecticut, Storrs, CT, 06269, United States

10 **Abstract:** The first national product of Surface Water Dynamics in France (SWDF) is generated on a
11 monthly temporal scale and 10-m spatial scale using an automatic rule-based superpixel (RBSP) approach.
12 The current surface water dynamic products from high resolution (HR) multispectral satellite imagery are
13 typically analyzed to determine the annual trend and related seasonal variability. Annual and seasonal time
14 series analyses may fail to detect the intra-annual variations of water bodies. Sentinel-2 allows us to
15 investigate water resources based on both spatial and temporal high-resolution analyses. We propose a new
16 automatic RBSP approach on the Google Earth Engine platform. The RBSP method employs combined
17 spectral indices and superpixel techniques to delineate the surface water extent; this approach avoids the
18 need for training data and benefits large-scale, dynamic and automatic monitoring. We used the proposed
19 RBSP method to process Sentinel-2 monthly composite images covering a two-year period and generate the
20 monthly surface water extent at the national scale, i.e., over France. Annual occurrence maps were further
21 obtained based on the pixel frequency in monthly water maps. The monthly dynamics provided in SWDF
22 products are evaluated by HR satellite-derived water masks at the national scale (JRC GSW monthly water
23 history) and at local scales (over two lakes, i.e., Lake Der-Chantecoq and Lake Orient, and 200 random
24 sampling points). The monthly trends between SWDF and GSW were similar, with a coefficient of 0.94.
25 The confusion matrix-based metrics based on the sample points were 0.885 (producer's accuracy), 0.963
26 (user's accuracy), 0.932 (overall accuracy) and 0.865 (Matthews correlation coefficient). The annual surface
27 water extents (i.e., permanent and maximum) are validated by two HR satellite image-based water maps and
28 an official database at the national scale and small water bodies (ponds) at the local scale at Loir-et-Cher.
29 The results show that the SWDF results are closely correlated to the previous annual water extents, with a
30 coefficient greater than 0.950. The SWDF results are further validated for large rivers and lakes, with
31 extraction rates of 0.929 and 0.802, respectively. Also, SWDF exhibits superiority to GSW in small water
32 body extraction (taking 2498 ponds in Loir-et-Cher as example), with an extraction rate improved by
33 approximately 20%. Thus, the SWDF method can be used to study interannual, seasonal and monthly
34 variations in surface water systems. The monthly dynamic maps of SWDF improved the degree of land
35 surface coverage by 25% of France on average compared with GSW, which is the only product that provides
36 monthly dynamics. Further harmonization of Sentinel-2 and Landsat 8 and the introduction of enhanced
37 cloud detection algorithm can fill some gaps of no-data regions.

38

39 **Keywords:** dynamic mapping, Google Earth Engine, Sentinel-2, water bodies, France, superpixel, spectral
40 indices, monthly

41 **1. Introduction**

42 *1.1. Background*

43 Water bodies are the main component of the land surface. The accurate spatial detection and dynamic
44 monitoring of inland water bodies are important tasks in many applications, such as sustainable land and
45 water management (Zou et al., 2017), water volume and water level estimation (Crétau et al., 2016;
46 Ohanya et al., 2013), natural hazard analysis (including flooding, drought, and urban inland inundation)
47 (Huber et al., 2013; Mueller et al., 2016), and local climate and zoology-related analysis (Huber et al., 2015;
48 Sun and Chen, 2012). Compared with conventional survey methods, remote sensing approaches monitor
49 water body dynamics in time- and cost-saving modes. Various types of remote sensing optical imagery (with
50 very high, high, and moderate spatial resolutions) have been utilized to monitor inland water bodies. (i)
51 Water body maps from very high-resolution (VHR) optical satellite imagery (Huang et al., 2015; C. Xie et
52 al., 2016) and aerial imagery (Ford, 2013) have fine spatial resolutions, but the data are expensive to obtain
53 and may not support long-term dynamic monitoring. (ii) The highly repetitive coverage of the Moderate
54 Resolution Imaging Spectroradiometer (MODIS) offers the possibility of dynamic monitoring every few
55 days (Che et al., 2017; Klein et al., 2014; Lu et al., 2018; Wang et al., 2014) , but the spatial resolution of
56 250 m is extremely coarse, especially for subtle variations in inland water bodies. (iii) High resolution (HR)
57 multispectral satellite remote sensing imagery balances temporal frequency and spatial resolution (Li and
58 Gong, 2016; Yésou et al., 2016) and has been commonly utilized because this imagery offers the following
59 advantages: vivid spectral information related to water characteristics (typically in the green, near infrared
60 (NIR), and short-wavelength infrared (SWIR) bands), an appropriate spatial resolution (tens of meters),
61 repetitive monitoring (i.e., nearly half a month), large-area coverage and free access.

62 Considerable effort has focused on extracting the seasonal and annual dynamics of the surface water
63 extent at large scales, typically using Landsat imagery (Li and Gong, 2016; Pekel et al., 2016; Tulbure et al.,
64 2016). However, inland surface water bodies are dynamically changing and undergoing severe drainage,
65 especially for ephemeral streams and lakes. Higher-resolution monitoring, such as using monthly time-series
66 analysis, can better capture the interannual variation in the surface water extent and presents the shrinking
67 and inundation that occurs during the year. Satellite-based monitoring of the monthly extent of surface water
68 bodies can integrate with hydrological models and meteorological data for further analyses.

69 Copernicus, the EU's Earth Observation Program, ensures the regular observation and monitoring of
70 Earth's sub-systems, including the atmosphere, oceans, and continental surfaces, and this program provides
71 reliable, validated and guaranteed information to support a broad range of environmental and security
72 applications and decisions. The HR optical component, the Sentinel-2 mission (Drusch et al., 2012),
73 acquires high spatial resolution optical observations (as high as 10 m) over global terrestrial surfaces with a

74 high revisit frequency (approximately five days) using a bi-satellite system, which is important for land
 75 cover dynamic mapping and updating. Sentinel-2 can effectively extract the distribution of land surface
 76 water at a resolution of 10 m (Du et al., 2016; Gong et al., 2019; Wang et al., 2018; Yang et al., 2018, 2017;
 77 Yésou et al., 2016), but its potential for dynamic water body monitoring and change detection deserves more
 78 attention considering the high revisit frequency of the satellite (Ogilvie et al., 2018a).

79 1.2. Related works

80 (1) Distribution of surface water

81 During the last 25 years, there have been many approaches to extract water bodies from multispectral
 82 imagery (Table 1 & Table 2). These approaches can be divided into three levels: pixelwise classification,
 83 object-based image analysis (OBIA) and subpixel fraction estimation. Pixelwise approaches directly extract
 84 the pixels associated with water body areas, mainly considering the spectral characteristics of targets. OBIA
 85 groups the adjacent pixels with similar features into homogeneous clusters, which provides valuable
 86 information, including spectral, textural, shape, and spatial relationships. Subpixel fraction estimation
 87 considers the mixed pixels in remote sensing images and estimates the fraction of water bodies in each pixel
 88 using the spectral mixture analysis (SMA) method. However, the relevant methodologies fall into two
 89 categories depending on whether training samples are needed. The sample-based approach relies on the
 90 training dataset for supervised classification at both the pixel and object levels or on pure endmember
 91 selection to derive the subpixel water body fraction. The rule-based approach is based on prior knowledge of
 92 the target and background instead of the known sample data.

93 Table 1. Methodologies of water body extraction from multispectral imagery

| Training samples | Different levels | Literature | Methodology | Main water bodies |
|---------------------------|-------------------------------------|--|---|--|
| Sample-based methods | Pixelwise supervised classification | (Acharya et al., 2016) | Decision tree | River and lakes |
| | | (Deng et al., 2017) | Decision tree | Urban lakes |
| | | (Isikdogan et al., 2017) | Deep learning | Inland surface water |
| | | (Mueller et al., 2016) | Regression tree | Across Australia |
| | | (Sun et al., 2015) | Support vector machines (SVMs) | Urban water bodies |
| | | (Tulbure and Broich, 2013) | Classification tree algorithm | Western Australia |
| | | (Verpoorter et al. 2012; 2014) | Supervised classification | Global lakes |
| | | (Jakovljević et al., 2018) | Supported vector machine (SVM) classifier | Open water bodies |
| | | (Tulbure et al., 2016) | Random forest | Australia |
| | | Object-based supervised classification | (Bayram, 2013) | Spectral indices |
| (Yang and Chen, 2017) | Spectral indices | | Urban water bodies | |
| Subpixel mixture analysis | Subpixel mixture analysis | (Pan et al., 2016) | Mixed land-water pixel extraction using SMA methods | Urban water bodies |
| | | (Rover et al., 2010) | Combined with regression-tree technique | Lakes, wetlands and small water bodies |
| | | (Zhou et al., 2014) | Spectral mixture analysis combined with multiscale extraction | Rivers |
| Rule-based methods | Spectral indices | (Arvor et al., 2018) | Time series indices | Small water reservoirs |
| | | (Avisse et al., 2017) | Water and vegetation indices | Small water reservoirs |
| | | (Campos et al., 2012) | Sample-based thresholding | Seasonal and permanent water |
| | | (Cian et al., 2018) | Minimum, maximum and mean of the NDVI throughout the entire stack of images | Flood mapping |
| | | (Du et al., 2016) | Indices and thresholding | Venice coastland |
| | | (Fisher et al., 2016) | Indices and thresholding | Eastern Australia |
| | | (Ogilvie et al., 2018) | New water index | Small water bodies |
| | | (Yamazaki et al., 2015) | Comparing popular water indices | Global water body map |
| | | (Yang et al., 2018) | Water indices and temporal analysis | Urban water bodies |

| | | | |
|-------------------------------------|--|--|--|
| | (Feng et al., 2016) | Refined by constrained energy minimization Terrain metrics and prior coarse-resolution water masks | Global inland water |
| Object/cluster-based image analysis | (Chen et al., 2017) (Mitkari et al., 2017) (Sivanpillai and Miller, 2010) (H. Xie et al., 2016) (Zhang et al., 2013) | Segment images using an active contour model Combined with band indices Unsupervised ISODATA algorithm to generate clusters k-means/ISODATA to generate clusters Object-oriented image analysis and edge detection | Glacial lake outlines Glacial lakes Water bodies Lake and river Coastlines |

94

95 Among the rule-based approaches, water indices and binary thresholding-based methods are
96 characterized by easy implementation and a high calculation efficiency and are thus widely utilized (Table
97 2), especially in large-scale and time series analyses (Campos et al., 2012; Pekel et al., 2016; Thomas et al.,
98 2015; Zou et al., 2017). Water indices differentiate the water bodies (normally with positive values) from the
99 background (tending to negative values). Many water indices have been designed to enhance the separation
100 between water bodies and other land cover types (Table 2). Water indices can be directly utilized for water
101 mapping based on thresholding (Allen and Pavelsky, 2018; Fan et al., 2018) and serve as the basis for other
102 algorithms, such as machine learning (Isikdogan et al., 2017), object-level segmentation (Mitkari et al.,
103 2017), and subpixel mapping (Zhou et al., 2014).

104

Table 2. Water indices designed for water body detection

| Water indices | Literature | Bands |
|---|--------------------------|--|
| normalized difference water index (NDWI) | (Gao, 1996) | NIR, SWIR |
| normalized difference water index (NDWI) | (McFeeters, 1996) | Green, NIR |
| modified NDWI (MNDWI) | (Xu, 2006) | Green, SWIR |
| automated water extraction index (AWEI) | (Feyisa et al., 2014) | Blue, Green, NIR, SWIRs |
| multi-spectral water index (WuWI) | (Wang et al., 2018) | Blue, Green, NIR, SWIRs |
| normalized difference mud index (NDMI) | (Bernstein, 2012) | Narrow bands with wavelengths of 795 nm and 990 nm |
| WI ₂₀₁₅ | (Fisher et al., 2016) | Green, Red, NIR, SWIRs |
| NDWI built-up index (NDWI-DB) | (Li et al., 2016) | Blue, SWIR |
| Tasseled Cap Wetness (TCW) | (Crist, 1985) | Blue, Green, Red, NIR, SWIRs |
| normalized difference vegetation index (NDVI) | (Zhu and Woodcock, 2012) | Red, NIR |
| NDWI _{nm} | (H. Xie et al., 2016) | Composed of a visible band and an infrared band |
| enhanced water index (EWI) | (Wang et al., 2015) | Green, Red, NIR, SWIR |
| simple water index (SWI) | (Malahlela, 2016) | Blue, SWIR |
| LBV transformation | (Zhang et al., 2017) | Green, Red, NIR, SWIR |

105

106 (2) Dynamics of surface water

107 Most previous large-scale and time series mapping studies of the surface water extent were conducted
108 based on MODIS and Landsat datasets (Aires et al., 2018), and the spatial resolution was generally 250 m or
109 30 m, respectively (Yésou et al., 2011). The dynamics of the surface water extent have been mapped at three
110 different time scales using Landsat data, including interannual, seasonal/inner-annual, and multi/bi-temporal
111 change analyses (Table 3). (i) Most works utilized Landsat series data to continuously monitor the general
112 trend of the surface water extent over several decades. Rokni et al. (2014) modeled the spatiotemporal
113 changes in Lake Urmia from 2000 to 2013 and reported a dramatic decreasing trend. Thomas et al. (2015)
114 mapped the inundation and flooding patterns of the Macquarie Marshes by selecting Landsat images (1989-

115 2010) over a range of flood magnitudes. Deng et al. (2017) monitored the extent of the spatiotemporal
 116 changes of a lake in Wuhan, China, based on Landsat images from 1987 to 2015. (ii) The seasonality of
 117 surface water based on interannual monitoring has also been widely explored. The most famous work was
 118 conducted by the European Commission’s Joint Research Centre (JRC) (Pekel et al., 2016), who developed
 119 high-resolution maps of the global surface water (GSW) occurrence, change, seasonality, and transition
 120 using Landsat data at 30 meter resolution. In addition, Campos et al. (2012) derived seasonal and permanent
 121 water data between 2007 and 2011 and monitored the decrease in water resources in Africa. Tulbure &
 122 Broich (2013) studied spatially and temporally explicit time series of a surface water body on the Swan
 123 Coastal Plain from 1999 to 2011 and adopted landscape metrics to determine the extent of changes in the
 124 seasonally continuous surface water body after comparing summer and winter images. Zou et al. (2017)
 125 generated four water body extent maps (maximum, year-long, seasonal, and average maps) of Oklahoma
 126 from 1984 to 2015 based on the annual water body frequency. (iii) Bi-/multitemporal images are typically
 127 applied to investigate flooding mapping and land use/cover (LULC) changes. Chignell et al. (2015) utilized
 128 pre- and post-flood Landsat 8 images to produce a flood layer image at the regional scale of the Colorado
 129 Front Range Flood in 2013. Bayram (2013) analyzed the combined shoreline and LULC changes of the
 130 Terkos Lake basin using Landsat satellite images from 1986, 2001, and 2009.

131 Table 3. Temporal scales for water body dynamics monitoring

| Temporal scale | Literature | Methodology |
|-------------------------|------------------------------|---|
| Annual to decade trend | (Allen and Pavelsky, 2018) | Water indices |
| | (Arvor et al., 2018) | Time series indices |
| | (Avisse et al., 2017) | Fmask, water and vegetation indices |
| | (Carroll and Loboda, 2017) | Using the DSWE product |
| | (Deng et al., 2017) | Indices and random forest |
| | (Fan et al., 2018) | Water index |
| | (Ogilvie et al. 2018) | Water index and hydrological modeling |
| | (Pardo-Pascual et al., 2012) | Shoreline subpixel detection |
| | (Sagar et al., 2017) | Median pixel compositing of NDWI stacks |
| | (Shi et al., 2017) | An ‘eight-field’ morphological method |
| | (Tseng et al., 2016) | Surface water area and level changes |
| | (Liu and Yue, 2017) | Band value and Otsu threshold |
| | (Zou et al., 2018) | The relationship between water and vegetation indices |
| (Yamazaki et al., 2015) | Spectral indices | |
| Seasonality | (Pekel et al., 2016) | Expert systems, visual analytics, and evidential reasoning |
| | (Tulbure and Broich, 2013) | Decision tree classification algorithm |
| | (Zou et al., 2017) | Spectral indices |
| | (Tulbure et al., 2016) | Random forest |
| | (Sheng et al., 2016) | Water index |
| Monthly changes | (Campos et al., 2012) | Water indices based on one image per month between 2001 and |
| | (Hui and Xu, 2008) | 2010 |
| | (Pekel et al., 2016) | Water indices and empirical threshold |

| | | Expert systems, visual analytics, and evidential reasoning |
|-----------------------|-------------------------|--|
| Multi- or bi-temporal | (Bayram, 2013) | OBIA and indices |
| | (Chignell et al., 2015) | Independent component analysis and indices |
| | (Ghosh et al., 2015) | Water index |
| | (Dronova et al., 2011) | OBIA |

132

133 Nonetheless, more fine-resolution temporal monitoring is necessary to reflect the subtle variabilities in
134 water bodies on a monthly scale. The monthly surface water occurrence based on multispectral imagery is
135 generally ignored. To our knowledge, monthly dynamics have only been assessed by Hui et al. (2008),
136 Dronova et al., (2011), Campos et al. (2012) and Pekel et al. (2016). Hui et al. (2008) monitored the monthly
137 changes in Poyang Lake, China, between November 1999 and October 2000, using eight images acquired
138 from Landsat ETM+ 5 and Landsat TM 7. Dronova et al. (2011) selected four images acquired in November
139 2007 and January, February, and March 2008 using the Beijing-1 microsatellite and examined the surface
140 cover composition and its changes at Poyang Lake. Campos et al. (2012) chose one image per month
141 between 2001 and 2010 to analyze the historical trend of the water bodies, and yet, these researchers could
142 not monitor the real-time changes in the water bodies. JRC GSW recorded the entire history of water
143 detection on a month-by-month basis between March 1984 and December 2018. However, the coverage of
144 the monthly map is still limited by an insufficient number of valid observations based on Landsat data.
145 Currently, the active Landsat 7 and 8 satellites theoretically allow an 8-day repeat coverage of the land
146 surface. However, on May 31, 2003, the scan line corrector (SLC), which compensates for the forward
147 motion of Landsat 7, failed and led to the loss of an estimated 22 percent of the dataset. Additional cloud
148 cover and haziness can reduce the number of valid images, which can result in a lack of sufficient data for
149 monthly dynamic mapping. Thus, the potential use of the Sentinel-2 constellation in water body monitoring
150 and dynamic analysis is a highly anticipated exploration.

151 *1.3. Contributions*

152 The main objective of this study is therefore to continuously monitor the monthly, quarterly and annual
153 changes in surface water body dynamics in France at a 10-m spatial resolution using Sentinel-2 imagery.
154 The main contributions of this study include developing an automatic methodology and application of the
155 method at the national scale.

156 First, an automatic rule-based superpixel (RBSP) approach is proposed. RBSP automatically analyzes
157 the large-scale spatiotemporal variability and trends of surface water bodies. A new spectral index-based
158 approach is proposed to delineate the water body extent. This method considers the different error sources in
159 water body detection: (i) built-up areas using an automated water extraction index (AWEI), with noise
160 associated with shadow and very-high albedo objects eliminated and (ii) natural areas using the normalized
161 difference muddy index (NDMI) (for muddy and shallow water bodies) and the AWEI, with noise
162 associated with vegetation ice and snow eliminated. Additionally, the proposed approach is implemented at
163 the superpixel level. Superpixel segmentation groups the connected pixels with similar characteristics, and

164 the automatic processing method is in accordance with the research objectives. RBSP is automatically run in
165 the Google Earth Engine (GEE) platform for large-scale dynamic mapping.

166 Second, the Surface Water Dynamics in France (SWDF) product is generated with monthly, quarterly
167 and annual surface water extents. To our knowledge, this product is the first national inland surface water
168 map published at the monthly temporal scale and a 10-m spatial scale. RBSP is applied to monthly and
169 quarterly images with medium composite pixels. Annual occurrence maps are further generated based on the
170 pixel frequency of the monthly water maps. Our product is evaluated in both the dynamic and static states
171 and at both national and local scales: (i) the monthly dynamic water maps are compared with satellite image
172 based water masks at the national scale (JRC GSW monthly water history) and at local scales (over two
173 lakes, i.e., Lake Der-Chantecoq and Lake Orient, as well as 200 random sampling points); (ii) the annual
174 surface water extent is validated by satellite image-based water maps (JRC GSW annual product and Theia
175 land cover product (Inglada et al., 2017)) and an official database (BD Carthage hydrological product, main
176 watercourses, and major lakes and reservoir) at the national scale and small water bodies (ponds) at local
177 scales (including the Sologne region of the Department of Loir-et-Cher).

178 **2. Methodology**

179 The methodology part involves the overall workflow (Figure 1) of the proposed RBSP approach and the
180 generated SWDF product. First, Sentinel-2 Level-1C data covering the France (Section 2.1) are collected.
181 Second, these images are preprocessed (Section 2.2) to eliminate the invalid pixels covered by clouds, to
182 divide the bu

183 ilt-up and natural scenes and to exclude the possible terrain shadows. Third, the proposed RBSP
184 approach is explained, including the different spectral rules for natural and built-up scenes in Section 2.3 and
185 superpixel technique to generate the homogeneous objects in Section 2.4. Finally, the auxiliary data and
186 metrics used to evaluate the generated SWDF product are described in Section 2.5.

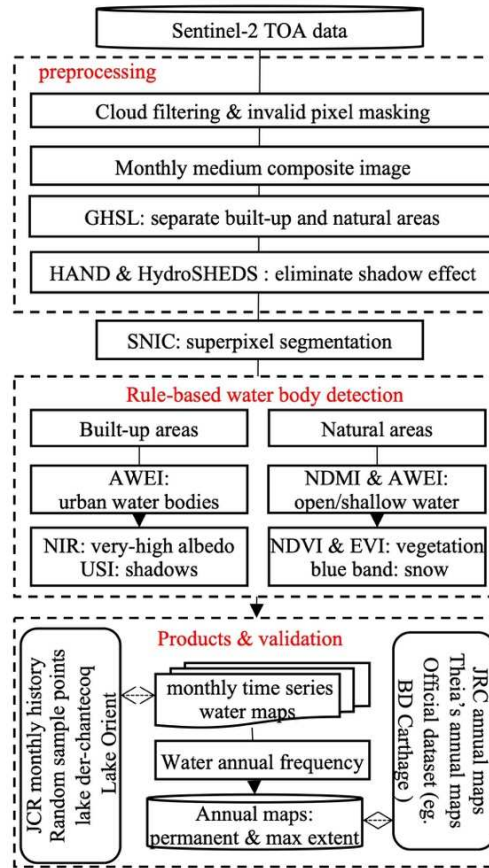


Figure 1. The workflow of the proposed RBSP approach and the validation of the obtained SWDF product

2.1. Study areas

The experiments presented in this paper focus on European France (i.e. mainland France and Corsica) (Figure 2), which encompasses an area of approximately 551,695 km². France lies within the northern temperate zone and mainly includes oceanic, semi-continental, Mediterranean, and mountain climates (Fort and André, 2013; Terasmaa et al., 2019). France possesses a wide variety of landscapes, from coastal plains in the north and west to the mountain ranges of the Alps in the southeast, as well as the Massif Central in the south and the Pyrenees in the southwest. Additionally, the islands of Corsica lie off the Mediterranean coast.

France has an extensive river system mainly consisting of four major rivers and their tributaries, including the Seine, Loire, Garonne and Rhône Rivers, with a combined catchment area that includes over 62% of the territory (Kristensen and Bogestrand, 1996). In addition, the Rhine River and some tributaries flow through the northeastern portion of the region. Knoema Corporation (2017) reported approximately 153,000 ha of inland water occupied by major rivers, lakes and reservoirs in France. Considering the water bodies larger than 1 ha, Bartout and Touchart (2013) regarded 555,000 waters bodies as corresponding to a cumulated surface area of 450,000 ha.

This study focuses on inland water detection and neglects coastline monitoring. The national and administrative boundaries are from GADM, the database of global administrative areas.

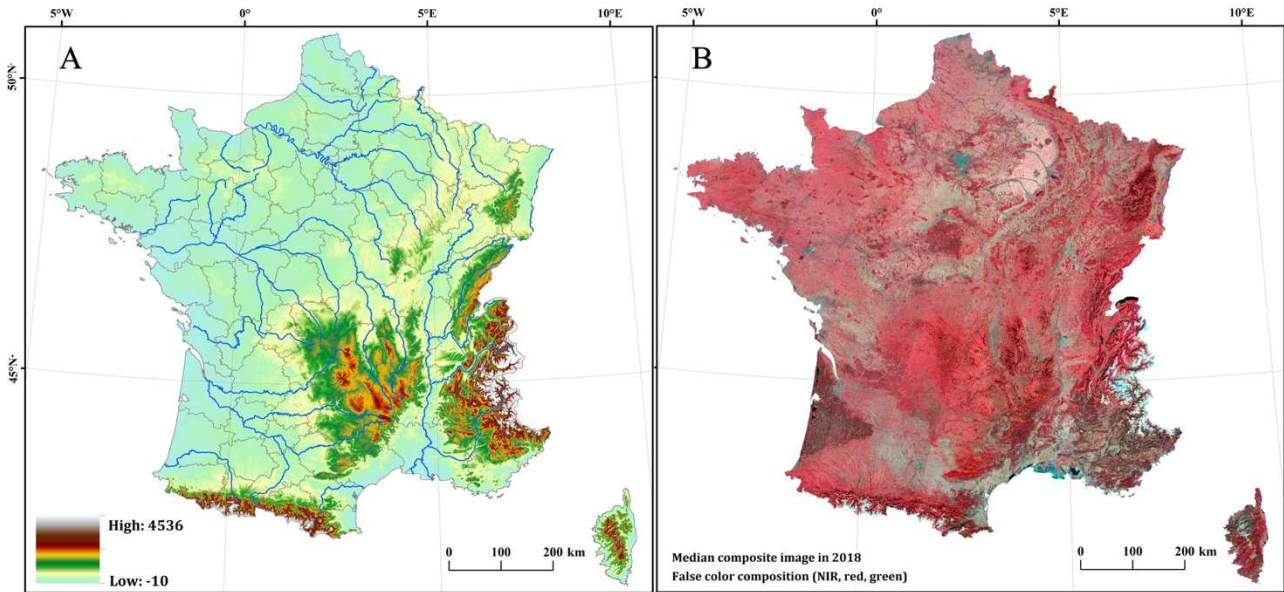


Figure 2. (A) The study area of France consists of 96 administrative divisions and (B) an example of a Sentinel-2 annual composite image

2.2. Datasets and GEE platform

This project uses the open source GEE as the research platform. The GEE provides programming and graphic interfaces for scientific applications using remote sensing data. With the powerful Google cloud storage and computational hardware technologies to accelerate remotely sensed data processing (Gorelick et al., 2017; Trianni et al., 2015), GEE is advantageous for large-scale mapping and time series analysis based on multispectral images, including analyses of surface water (Pekel et al., 2014), forest cover (Hansen et al., 2013), paddy rice planting areas (Dong et al., 2016), and settlement areas (Huang et al., 2017).

The Sentinel-2 mission is composed of a two-satellite system, Sentinel-2A and Sentinel-2B, which were launched on 23 June 2015 and 07 March 2017 respectively, allowing for a high revisit frequency of approximately 5 days at the equator and 2-3 days at the mid-latitudes. The high revisit frequency is important for dynamic land cover mapping and monitoring. Sentinel-2 imagery includes 13 spectral bands (Table 4) that span from the visible (VIS) and near infrared (NIR) bands to the shortwave infrared (SWIR) bands at different spatial resolutions on the ground ranging from 10 m to 60 m (Drusch et al., 2012). In this study, six broad bands, including the VIS, NIR, and SWIR bands, and two narrow bands, the Red Edge 3 and 4 bands, are utilized. The SWIR and Red Edge bands with a spatial resolution of 20 m were resized to 10 m by dividing each pixel into 4 pixels with the same gray value to maintain the same spatial resolution as the VIS and NIR bands.

Table 4. Band information of the Sentinel-2 Level-1C data

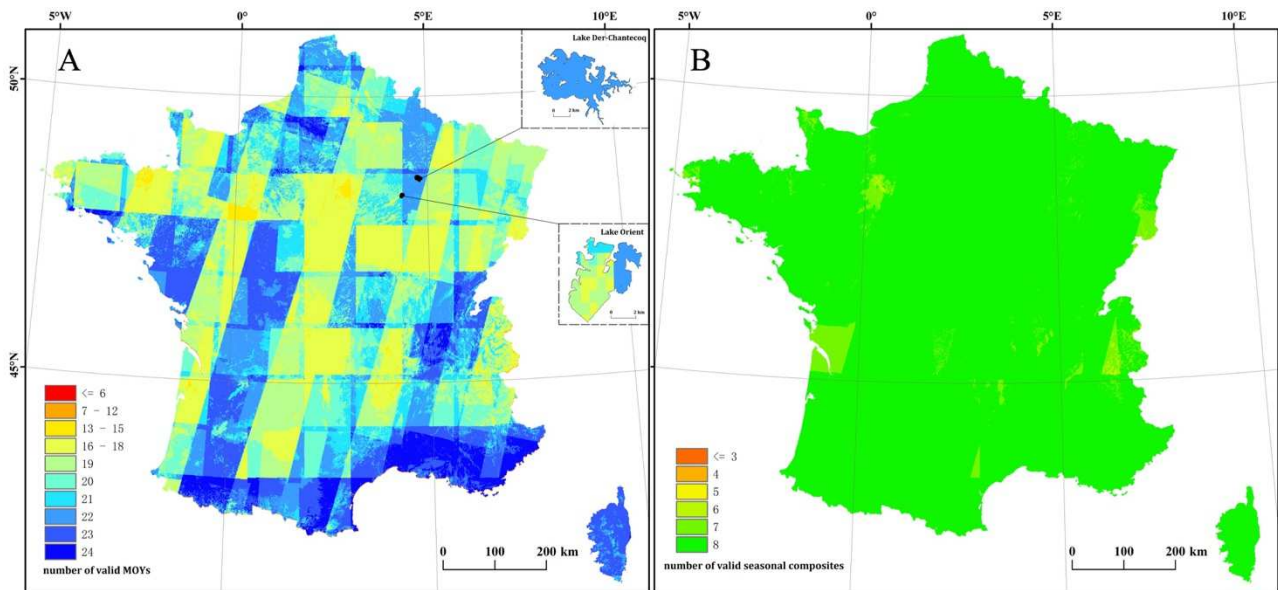
| Band number | Band name | Resolution (m) | Band number | Band name | Resolution (m) |
|-------------|-----------|----------------|-------------|------------|----------------|
| B1 | Aerosols | 60 | B8 | NIR | 10 |
| B2 | Blue | 10 | B8A | Red Edge 4 | 20 |

| | | | | | |
|----|------------|----|------|-------------|----|
| B3 | Green | 10 | B9 | Water vapor | 60 |
| B4 | Red | 10 | B10 | Cirrus | 60 |
| B5 | Red Edge 1 | 20 | B11 | SWIR 1 | 20 |
| B6 | Red Edge 2 | 20 | B12 | SWIR 2 | 20 |
| B7 | Red Edge 3 | 20 | QA60 | Cloud mask | 60 |

227 The Sentinel-2 Level-1C dataset is the standard product for top of the atmosphere (TOA) reflectance and
 228 has been completely integrated into the GEE platform. A QA60 band is embedded in the Sentinel-2 Level-
 229 1C data, where opaque and cirrus clouds are computed based on spectral criteria. In the project, the Sentinel-
 230 2 images are filtered and collected with less than 20% cloud cover. Because the current QA60 band cannot
 231 provide accurate cloud and cloud detection results, we select a low cloud cover threshold (20%) to reduce
 232 the potential of including omission errors in cloud/cloud shadow detection.

233 Here, we used 8955 Sentinel-2 images (based on the 20% maximum cloud criteria) and analyzed an
 234 average of 373 Sentinel-2 observations for each month. Then, the QA60 band associated with the image was
 235 used to exclude the invalid pixels in each image. These images were acquired between March 2017 and
 236 February 2019 to cover the four seasons (starting on March 1, June 1, September 1, and December 1 for
 237 spring, summer, autumn and winter, respectively) during a two-year period. The annual map covers four
 238 quarterly datasets starting on March 1.

239 To complete the task of Month-Of-Year (MOY) time series analysis, images were placed into collections
 240 according to the calendar month. Image composition combines spatially overlapping images into a single
 241 image that has a medium value for each band within the monthly collection. Figure 3A displays the number
 242 of valid monthly composites of 24 months, which is the occurrence of available monthly surface water maps.
 243 The proposed RBSP approach processes these 24 monthly time series composite data between March 2017
 244 and February 2019 and generates the SWDF product. Over half of the land surface has been covered with
 245 over 20 MOYs, and over 90% percentage of the land surface is covered with over 17 MOYs. If utilizing
 246 quarterly composites, approximately 96% percentage of the land surface is covered with all eight seasons
 247 (Figure 3B). The detailed statistics of the valid MOYs and quarterly composites can be found in the
 248 Supplemental materials (Figure S3 and Figure S4). That is, a short period of monthly analyses may result in
 249 the occurrence of data gaps but are beneficial for observing the visible changes in hydrology in a higher
 250 temporal resolution.



251
 252 Figure 3. Number of valid MOYs (A) and quarterly composites (B) during a two-year period using Sentinel-2 with less
 253 than 20% cloud cover

254 The auxiliary data include the JRC Global Human Settlement Layer (GHSL), HydroSHEDS, and Height
 255 Above the Nearest Drainage (HAND) datasets, all of which are available globally and have been integrated
 256 into the GEE platform. The GHSL contain multitemporal information layers on built-up areas, as derived
 257 from Landsat image collections (1975, 1990, 2000, and 2015) (Pesaresi et al., 2015). The latest built-up
 258 layer in 2015 was utilized to separate built-up and natural areas, and water delineation issues stemmed from
 259 different error sources (Yang et al., 2018).

260 Notably, terrain shadows are easily misclassified as water bodies, and digital elevation models (DEMs)
 261 are widely used to exclude terrain shadow effects. Two hydrologically relevant terrain models, HAND
 262 (Donchyts et al., 2016b; Silveira et al., 2011) and HydroSHEDS (Lehner and Döll, 2004), were utilized to
 263 eliminate mountain shadow effects. Both models are based on high-resolution SRTM elevation data and are
 264 generally used in hydrological and remote sensing applications, such as water likelihood elimination and hill
 265 shadow correction. In this study, HydroSHEDS was used to mask mountain areas with slopes greater than 5
 266 degrees. HAND was used to mask terrain shadow areas in flat regions with a threshold of 30 (Table 5).

267 *2.3. Rule-based water body detection*

268 Spectral indices highlight the pixels of objects of interest from the background, and binary thresholding
 269 can be used to delineate the object areas, which benefits time series and large-scale analyses due to the ease
 270 of implementation. Water body mapping based on water indices faces error identification, and the main
 271 noise source varies with different indices (such as the NDWI, MNDWI, and AWEI) and backgrounds
 272 (mainly including vegetation, shadows, snow and built-up objects) (Yang et al., 2018). Compared to natural
 273 and open areas, the urban environment consists of heterogeneous human-made objects and can lead to the
 274 severe overestimation of water bodies. In this study, the AWEI, a water index for urban scenes (Feyisa et al.,
 275 2014), is adopted to distinguish water bodies from the background. However, the AWEI still faces some

276 challenges; for example, the omission error of muddy and shallow water bodies widely can be considerable
 277 in natural areas, and commission error can occur due to the existence of building shadows and high-albedo
 278 objects in urban areas. The study area is thus divided into natural/open scenes and urban/built-up scenes to
 279 address the different types of error sources. The GHSL settlement regions designated in 2015 (Pesaresi et al.,
 280 2015) are adopted to separate the natural and built-up areas, which were further processed with different
 281 rules (Table 5).

282 Table 5. The image characteristics used to delineate water bodies from the background using Sentinel-2

| Scenes | Feature | Equation or Methodology | Thresholding | Objectives |
|----------------|--------------------|---|---|--------------------------------|
| Preprocessing | HydroSHEDS | HydroSHEDS.slope | Empirical value: 5 | Terrain shadows |
| | HAND | Combined with JRC water occurrence | Empirical value: 30 | Mountain shadows in flat areas |
| Built-up areas | AWEI _{sh} | $B2 + 2.5 \times B3 - 1.5 \times (B8 + B11) - 0.25 \times B12$ | Edge-based Otsu | Water maps |
| | NIR band | B8 | Empirical threshold: 0.2 | Very-high albedo noise |
| | USI | $\frac{-2}{(1 - B2) \times (1 - B3) \times (1 - B4)}$ | Edge-based Otsu | Urban shadow noise |
| Natural areas | MWI | $\max\{NDMI, AWEI_{sh}\}; NDMI = \frac{B7 - B8A}{B7 + B8A}$ | Edge-based Otsu | Water maps |
| | MVI | $MVI = \frac{EVI + NDVI}{2}; NDVI = \frac{B8 - B4}{B8 + B4};$ $EVI = \frac{2.5 * (B8 - B4)}{(B8 + 6 * B4 - 7.5 * B2 + 1)}$ | Relative threshold $MVI - MWI > 0.1$ | Vegetation noise |
| | Blue band | B2 | Empirical threshold: 0.5 | Ice and snow noise |

283 Natural areas may include muddy and shallow water bodies, especially after rainfall events, and these
 284 areas could be underestimated by the AWEI. The NDMI (Bernstein, 2012) is often utilized to highlight
 285 muddy and shallow water pixels, and it was originally designed as a filter to exclude those pixels and
 286 improve the accuracy of quick atmospheric correction (QUAC). Thus, a mixed water index (MWI) with
 287 large AWEI and NWI values is used to reflect the surface water extent in the natural environment. Moreover,
 288 vegetation indices can suppress shadow effects (Yamazaki et al., 2015) and vegetation misclassification
 289 (Zou et al., 2017) in water body extraction. In this study, a mixed vegetation index (MVI) is used to
 290 eliminate errors in the surface water extent, and only those pixels that meet the criteria ($MVI - MWI \leq$
 291 0.1) are classified as open surface water body pixels. Additionally, ice and snow generally display a very
 292 high degree of reflection at visible wavelengths and low reflection in the NIR and SWIR band. That is, ice
 293 and snow have a similar spectral trend (from VIS to NIR and SWIR) as water bodies, except for its stronger
 294 reflectance in the VIS bands. Thus, the blue band (greater than 0.5) is used to exclude ice and snow cover in
 295 mountainous areas.

296 Urban scenes involve heterogeneous human-made objects, where some building shadow areas and very-
 297 high albedo objects may return high positive values after AWEI calculations and serve as the main noise
 298 sources for water body maps. The NIR band is used to eliminate very-high albedo objects considering the
 299 ultralow reflectance of water bodies. Although the AWEI can suppress low-albedo objects and shadows in

300 urban scenes, the misclassification of shadow areas still cannot be avoided. Thus, we designed an urban
301 shadow index (USI) to highlight the shadows in urban scenes. The index considers the low reflectance of
302 shadow areas in VIS bands compared to that of water bodies, and the reflectance values of both types of
303 objects tends to zero in the NIR and SWIR bands.

304 The binary segmentation threshold is an important factor when using spectral indices to delineate target
305 objects. The imaging of spectral indices involves polarization, where the pixel values of an object of interest
306 tend to be positive and the background returns negative values in theory. The histogram of an index image is
307 thus characteristic of a bimodal distribution representing the object and background and a deep and sharp
308 valley between two peaks. Although a user-defined threshold can return optimum results, it is more
309 appropriate to use an automated threshold or an empirical threshold to automate the delineation process,
310 especially for large-scale and time series analyses.

311 In this paper, an improved Otsu threshold is adopted based on the Canny edge detection algorithm
312 (Donchyts et al., 2016a). The performance of the global thresholding techniques (including Otsu's method)
313 used for binary segmentation is limited for small objects and images with abundant noise (Lee et al., 1990).
314 Land surface water represents a small fraction of the land cover in some administrative divisions in France.
315 Thus, the Canny edge detection algorithm is first used to identify the pixels within the buffer areas of each
316 edge. A histogram-based Otsu approach is then applied to these pixels to filter low-probability water bodies
317 in the scene. In addition, several soft empirical thresholds are adopted to exclude error sources to some
318 extent. Although some pixels of these land cover types (such as snow, very-high albedo objects and
319 vegetation) may return values similar to those of water bodies after water index calculation, they exhibit
320 differences in other spectral bands and indices. Thus, soft empirical thresholds can effectively reduce
321 overestimation issues. Table 5 lists the specific thresholds for different objects. For example, very-high
322 albedo masking is given a loose threshold of 0.2 because water bodies absorb most of the spectral energy,
323 whereas high-albedo objects have strong reflectance.

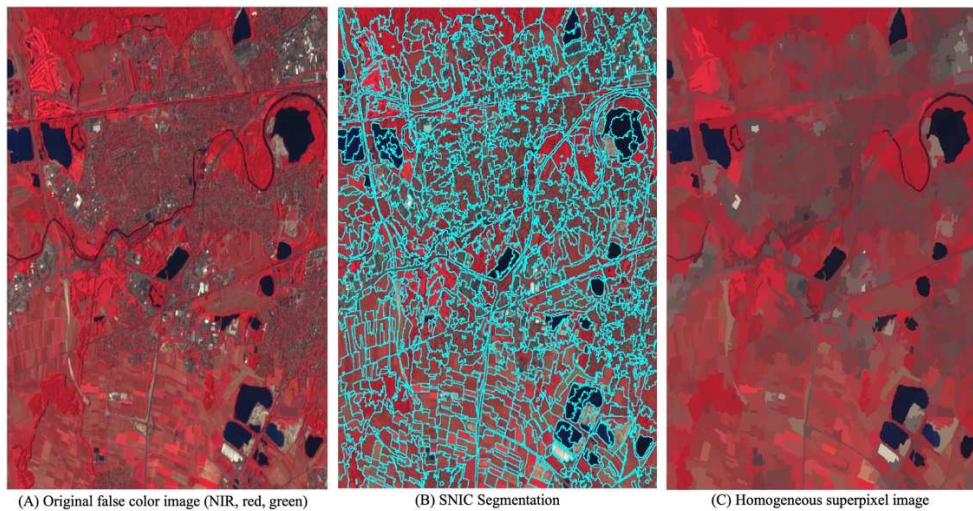
324 *2.4. Superpixel water body mapping*

325 Due to the lack of consideration of contextual information, the water body thematic maps obtained at the
326 pixelwise level often experience a “salt and pepper” problem with sparse noise (Yang and Chen, 2017;
327 Zhang et al., 2015). Rather than concentrating on individual pixels, OBIA groups the nearby pixels with
328 similar characteristics as homogeneous clusters (Fernández et al., 2014; Huang et al., 2015; Mitkari et al.,
329 2017), which can effectively restrain the “salt and pepper” phenomenon and convey valuable information,
330 including the spectral, textural, shape, and spatial information associated with adjacent objects. However,
331 OBIA can be time consuming when extracting information from large images because most segmentation
332 algorithms use the pixel grid as the initial object representation (Stutz et al., 2018). Additionally, automatic
333 segmentation remains an unresolved problem because segmentation is sensitive to many factors, such as the
334 image sensor resolution, scene complexity and number of bands (Csillik, 2017; Gong et al., 2017).

335 In the field of computer science, superpixel segmentation has become increasingly popular, and images
336 are divided into hundreds of non-overlapping superpixels (Ren and Malik, 2003). Similar to OBIA, a
337 superpixel is composed of pixels that are spectrally similar and spatially adjacent, and a superpixel is the
338 basic unit for subsequent processing steps. Compared with OBIA, superpixel segmentation can be
339 performed automatically for large-scale remote sensing images with low memory requirements and few
340 parameters.

341 In the proposed framework, a simple non-iterative clustering (SNIC) algorithm (Achanta and Ssstrunk,
342 2017) is applied to generate the corresponding superpixel blocks. The SNIC algorithm is an improved
343 version of the simple linear iterative clustering (SLIC) algorithm (Achanta et al., 2012) and is a fast and
344 powerful algorithm with high boundary adherence and low complexity (Gharibbafghi et al., 2018). The
345 SNIC algorithm has been proven to perform better and faster than other state-of-the-art superpixel
346 algorithms with less memory in comparisons based on segmentation benchmarks (Achanta and Ssstrunk,
347 2017). This study aims to automatically and rapidly monitor water body dynamics. SNIC is thus selected
348 due to its speed and ability to perform well for various study sites with a single set of default parameters.

349 The main parameter of SNIC is compactness. A large value of compactness reflects clusters with a
350 generally rectangular shape. In this study, a low compactness value (0.1) is selected considering the irregular
351 shape of surface water bodies. Superpixels are composed of clustered individual pixels (Figure 4), and the
352 corresponding mean value can be used as an input for the rule-based superpixel water body delineation
353 algorithm (Table 5). This approach results in a fast, simple, and efficient computation.



355 Figure 4. SNIC segmentation to generate a homogeneous superpixel image using the mean value of the pixels within a
356 block

357 2.5. Validation and comparison

358 A statistically rigorous validation for this product would be desirable. However, a statistically robust
359 national validation dataset is not available to measure the accuracy of this national water body database,
360 especially considering the extent of surface water dynamics. Nonetheless, we evaluated our product with
361 other existing global, national and local datasets (see S.2 in the Supplemental materials for the available

362 online addresses). We also performed a qualitative assessment based on careful visual interpretation (see S.3
 363 in the Supplemental materials and attached Data). Table 6 lists the main reference datasets from HR satellite
 364 image-derived water masks and official databases and the evaluation metrics.

365 Table 6. Datasets used to evaluate SWDF monthly and annual surface water maps at national and local scales

| | | Monthly dynamic map | | Annual static map | |
|----------|-------------------------------|--|--|--|--|
| | | Dataset | Evaluation | Dataset | Evaluation |
| National | Satellite image based product | JRC GSW monthly water history | Correlation analysis & trend analysis | Theia OSO annual product JRC GSW annual product | Confusion matrix & correlation analysis |
| | Official database | Not available | | BD Carthage in 2016 Main watercourse Main lake and reservoir | Confusion matrix Extraction rate Extraction rate |
| Local | Satellite image based product | 200 random sample points Two seasonal lakes South coastal area | Confusion matrix Trend analyses Qualitative analyses | Small water bodies in Loir-et-Cher provided from JRC GSW | Comparison based on confusion matrix & number count |
| | Official database | Not available | | Small water bodies in Loir-et-Cher | Confusion matrix & Number count |

366

367 (1) Evaluation metrics

368 The monthly and annual surface water extents are evaluated considering classification of water bodies
 369 and estimation of area extent. The classification accuracy of water body pixels is measured by the confusion
 370 matrix and detection rate (τ). Except for the distribution of the water bodies, it is important to estimate the
 371 amount of the surface water bodies. Based on sine and cosine fitting, a MOY model is used to predict the
 372 tendency of the monthly surface water area. Linear regression and the correlation coefficient are also used to
 373 quantitatively analyze the consistency of the surface water area estimation.

374 The confusion matrix divides the pixels in the study area into four classes: TP (true positive), FN (false
 375 negative), FP (false positive), and TN (true negative), reflecting accurate pixel extraction, missing water
 376 bodies, inaccurate extraction, and the accurate rejection of non-water, respectively. Four normalized metrics
 377 (Eq. 1) were then calculated to assess the performance of the proposed approach. The producer's accuracy
 378 (PA) and user's accuracy (UA) were used to indicate completeness and correctness, respectively. A low PA
 379 reflects serious omission error, and a low UA indicates an extreme commission error. The accuracy (ACC)
 380 and Matthews correlation coefficient (MCC) indicate the general accuracy of the approach. In this study, the
 381 extents of surface water and non-water bodies may be unbalanced and vary greatly. The MCC considers the
 382 four confusion matrix categories and is thus more informative than the ACC, especially when the water
 383 bodies account for a small portion of the environment.

384
$$PA = \frac{TP}{TP+FN}, UA = \frac{TP}{TP+FP}, ACC = \frac{TP+TN}{TP+FN+FP+TN}, MCC = \frac{TP*TN-FP*FN}{\sqrt{(TP+FP)(TP+FN)(TN+FP)(TN+FN)}} \quad (1)$$

385 A detection rate (τ) is used to measure how well the extent (for lake) or length (for river) is accurately
 386 extracted. τ is the ratio of the correctly extracted extent (for lake) or watercourse (for river) to the

387 corresponding value in the reference dataset (Eq. 2). The extracted watercourse is calculated through an
 388 intersection process with the buffering area of the experimental river extent considering the positional
 389 deviation of the reference dataset.

$$390 \quad \tau = \frac{\text{Product}(\text{area}/(\text{buffer area})) \cap \text{Reference}(\text{Area}/\text{length})}{\text{Reference}(\text{area}/\text{length})} \quad (2)$$

391 The monthly surface water area model is a function of the sines and cosines shown in Eq. (3), and it is
 392 initially used to predict the day-of-year (DOY) time series surface reflectance for Landsat data (Zhu et al.,
 393 2012; Zhu and Woodcock, 2014). In this study, we utilize the monthly composite image to simulate the
 394 month-of-year (MOY) time series of the surface area. The sine and cosine models estimate the interannual
 395 seasonal changes and inner-annual trend simultaneously, and these variations are in accord with the land
 396 surface water dynamics. A few coefficients are required to fit the functions considering the relatively small
 397 number of monthly composites. The generalized reduced gradient (GRG) solution method (Lasdon et al.,
 398 1978) is used to fit the nonlinear time series model.

$$399 \quad \hat{p}(\Delta m)_{GRG} = a_0 + a_1 \sin\left(\frac{2\pi}{12} \Delta m\right) + b_1 \cos\left(\frac{2\pi}{12} \Delta m\right) + a_2 \sin\left(\frac{2\pi}{12 \times N} \Delta m\right) + b_2 \cos\left(\frac{2\pi}{12 \times N} \Delta m\right) \quad (3)$$

400 where Δm is the month number of the sequence, N is the number of years of utilized Sentinel-2 data, a_0
 401 is the coefficient for overall values, a_1 and b_1 are the coefficients of inner-annual change, and a_2 and b_2 are
 402 the coefficients of interannual change.

403 Additionally, a linear regression and the correlation coefficient were used to evaluate the spatial
 404 distribution (in the units of 96 administrative divisions) of the surface water and the general trend (monthly
 405 change) of the surface water area. The correlation (a value between -1 and $+1$) is a common numerical
 406 measure of the degree of similarity or linear association between two variables. In this study, the Pearson
 407 correlation coefficient (r) (Eq. 4) was adopted to measure the consistency of the extent area prediction based
 408 on two products. The higher the positive value is, the more similar between the two results are in the
 409 estimation of the surface water area.

$$410 \quad r = \frac{\sum_{d=0}^{96} (p_d - \bar{p})(r_d - \bar{r})}{\sqrt{\sum_{d=0}^{96} (p_d - \bar{p})^2 \sum_{d=0}^{96} (r_d - \bar{r})^2}} \quad (4)$$

411 where d is the administrative division in France, and p_d and r_d are the surface water areas within the
 412 division estimated by our SWDF product and previous products (GSW and OSO), respectively.

413 (2) National scale datasets

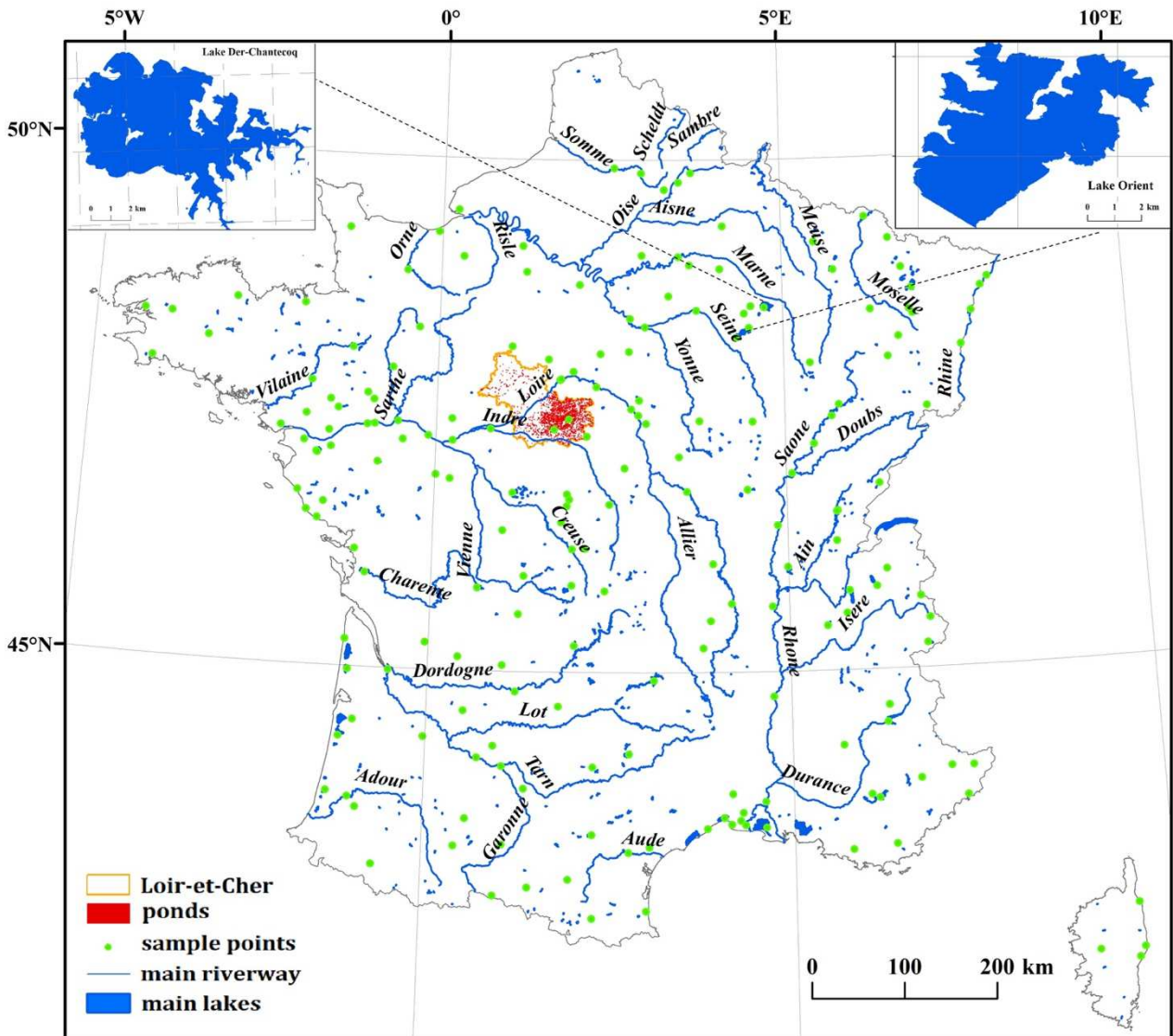
414 Two HR satellite derived water masks and some official datasets at the national scale are available to
 415 evaluate the SWDF results.

416 JRC GSW used 3,865,618 scenes (till now) from Landsat 5, 7, and 8 to quantify global water body
 417 dynamics from March 1984 to December 2018, at a 30-m spatial resolution, with an overall accuracy over
 418 90%. GSW is currently the only product providing monthly dynamic data for inland surface water at a
 419 spatial resolution of several decameters. Thus, a detailed comparison of the monthly dynamics and annual
 420 surface water map in 2017 and 2018 from GSW and SWDF is conducted in this project.

421 The French Theia Land Data Centre has set up a Scientific Expertise Centre OSO (“Occupation des sols”
422 in French) group, and the aim is to produce a land cover map of France using Sentinel-2 images. The OSO
423 product is updated once a year, with the inland surface water extent at a 10-m resolution; the annual surface
424 water extent from 2016-2018 has been released (Inglada et al., 2017). The overall accuracy of land
425 classification is approximately 90%, and the F-score for the surface water is approximately 0.99. The
426 consistency of annual water maps in 2017 and 2018 from SWDF and OSO are compared by using a
427 confusion matrix and correlation analysis.

428 The national hydrological surface of the BD Carthage database provided by IGN, the French National
429 Institute of Geography, drew the surface water extent in 2016. BD Carthage is used to evaluate the
430 maximum annual water extents in 2017 and 2018 in the SWDF product using confusion matrix-based
431 metrics. However, the different years between BD Carthage and SWDF mean that the surface water may
432 vary in terms spatial distribution.

433 Other hydrological datasets are also used to evaluate the extraction rates (τ) of the main rivers and lakes
434 in the SWDF annual surface water maps (Figure 5). The watercourses of the major rivers in Europe, with a
435 catchment area larger than 5,000 km², released by European Environmental Agency, and the surface extents
436 of the main lakes and reservoirs published by Système d’Information sur l’Eau (SIE) are used as the
437 reference maps.



438
 439 Figure 5. Reference data used to evaluate the water body maps, which involve the publicly released datasets (main
 440 rivers and lakes, and ponds in Loir-et-Cher) and a detailed monitoring analysis (Lake Der-Chantecoq and Lake Orient,
 441 as well as 200 sample points)

442 (3) Local scale datasets

443 Three local approaches have been carried out. The first approach corresponds to the analysis of 200
 444 samples points' analysis, the second approach compares the monthly surface water dynamics with a detailed
 445 Sentinel-2 time series over the two major reservoirs of Lake Der-Chantecoq and Lake Orient (Figure 5), and
 446 the third approach considers a large number of ponds in the Sologne region of the Loir-et-Cher Department.
 447 The detailed information and vector datasets of the sample points and these two reservoirs are provided in
 448 the Supplemental materials (S.3) and attached Data files.

449 To validate the monthly time series of surface water dynamics, we estimated confusion matrices based
 450 on 200 sample points (green points in Figure 5), which were selected from a stratified random sampling
 451 design using water/non-water strata and monthly time series of Sentinel-2 composite images. A pixel could
 452 alternate among water, non-water and no-data over the time series, and a careful visual interpretation is
 453 likely the most stable approach other than long-term field work. The accuracy of the surface water time

454 series was described by summarizing the data in a confusion matrix and estimating the normalized
455 coefficients (Eq. 1) of water/non-water samples across France.

456 The reservoirs, Lake Der-Chantecoq, 48 km², and Lake Orient, 23 km², (enlarged views in Figure 5) are
457 the largest and third-largest artificial lakes in France, respectively. The Lake Der-Chantecoq and Lake
458 Orient reservoirs are designed to protect Paris from floods by holding the water of the Marne River and
459 Seine River, respectively. These reservoirs are fully controlled; infilling occurs from November to June, and
460 at that time, water is taken from the Marne River (for Lake Der-Chantecoq) and the Seine (Lake Orient).
461 From July to October, water is released from the reservoirs for flow replenishment of the rivers. Surface
462 water changes dramatically during the year, reducing by half of the original extent from the high to low
463 period for Lake Der-Chantecoq and reducing to a fourth of the original extent for Lake Orient. During the
464 period of March 2017 to February 2019, 46 and 49 Sentinel-2 images were selected over Lake Der-
465 Chantecoq and Lake Orient, respectively. One Landsat-8 image acquired on December 7, 2017, is used
466 because of no clear Sentinel-2 image is available. We generated the reference data of these two lakes using
467 an SVM classification approach and an on-screen quality check.

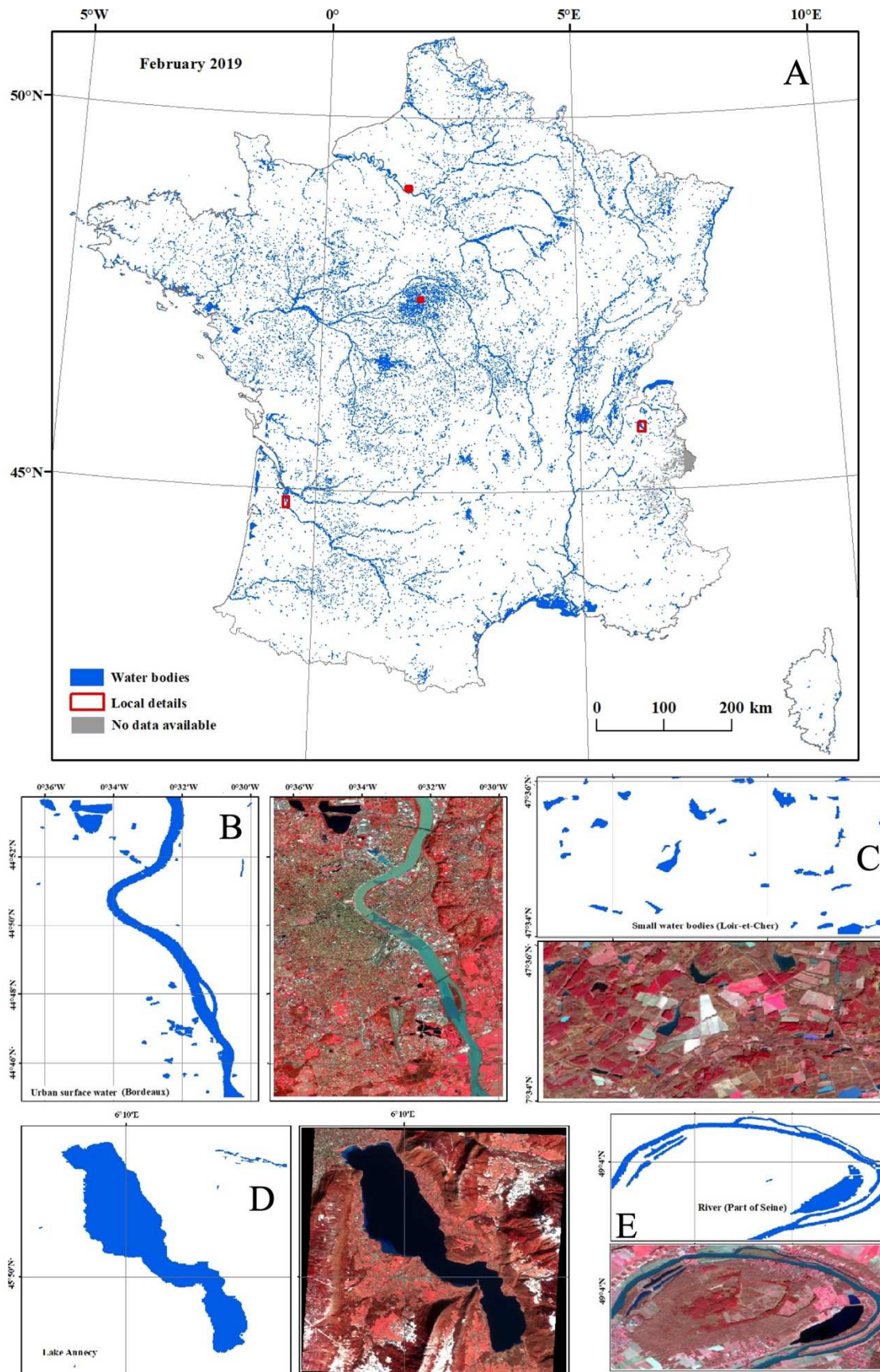
468 Additionally, the Sologne region, which is a wet and relatively wild area located in the southern portion
469 of Loir-et-Cher Department, is characterized by a large number of ponds, with a total of approximately
470 3,200 ponds, for a total surface area of 12,000 ha. These ponds correspond to small water bodies, where
471 only 50 water bodies reach an area of 50 ha and the largest pond has an area of 180 ha. The reference dataset
472 for these ponds released by the Departmental Direction of the Territories (DDT) is used to evaluate the
473 accuracy of the proposed approach for small water body detection using the confusion matrix.

474

475 **3. Results**

476 *3.1. Monthly and quarterly dynamics of the surface water extent*

477 The development of a consistent and automated RBSP workflow enables us to generate a national-scale
478 SWDF product (vector format products are attached in the Supplemental materials and Data files). We
479 generate the spatiotemporal dynamics of inland surface water bodies using monthly composite images
480 extending from March 2017 to February 2019. Figure 6 displays the land surface water extent in France in
481 February 2019. The detailed results include the urban areas in Bordeaux, the natural environment of forest
482 and farmland near Paris and in Loir-et-Cher, and the mountainous area by the Alps. Correspondingly, the
483 land surface water bodies involve the Garonne River, which runs through Bordeaux; the Seine River, which
484 flows through natural areas; small water bodies, such as ponds, that are surrounded by farmlands; and Lake
485 Annecy, which is located in alpine area with terrain shadow and snow. These different types of water bodies
486 and backgrounds reflect the robustness of the RBSP and the effectiveness of the SWDF analysis method.



487

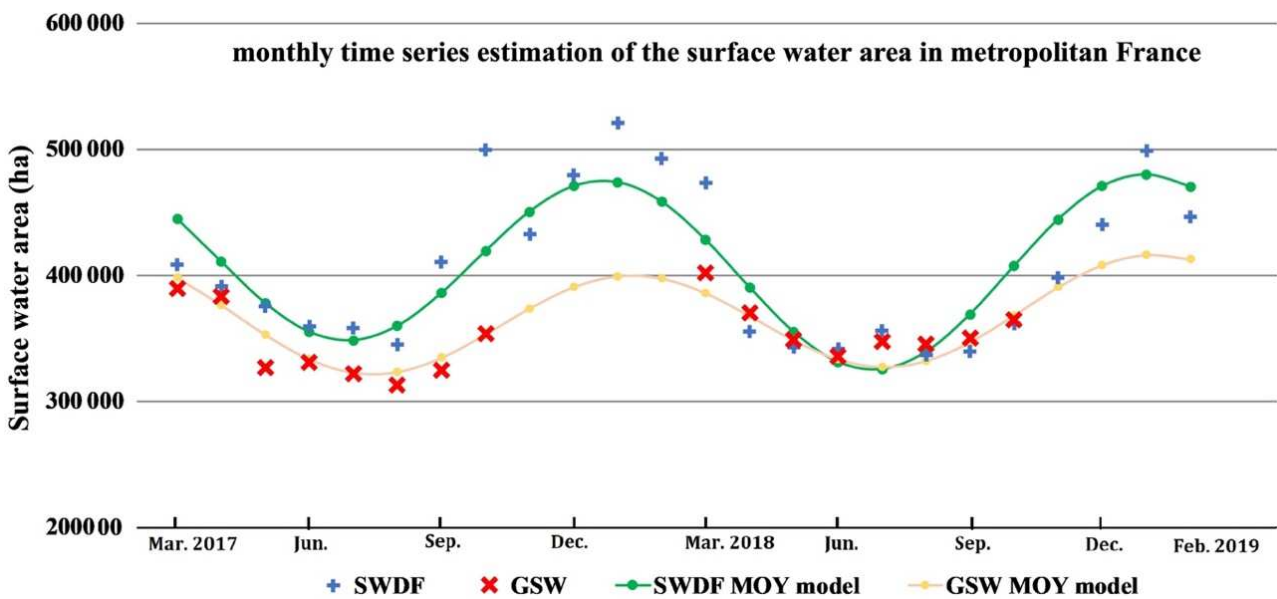
488

489

Figure 6. Surface water extent using monthly composite data during February 2019 (A) in France and several details over different environment/landscape units, including (B) urban, (C) agricultural, (D) mountainous and (E) forest areas.

490

491 As the only two available products recording the monthly variation in surface water extent, SWDF and
492 GSW are compared in terms of the aspect of area predictions. We construct two MOY time series models
493 based on the monthly surface water area calculated in the SWDF (at the annual scale) and GSW (between
494 March and October) products, and then, we evaluate the predicted trends based on sine and cosine fitting
495 (Figure 7). Both products exhibit similar seasonal trends, and the correlation coefficient of the variation is
496 0.940. However, SWDF provides more of the larger surface water area than GSW, and this average increase
497 of approximately 35,000 ha is related to the gain of the spatial resolution from the 30 m of Landsat image to
498 the 10 m of Senitnel-2 image.



499

500 Figure 7. Tendency of national MOY surface water area variations estimated from the SWDF and GSW products. The
501 crossing points indicate the monthly surface water area of France, and the curves present the fitted seasonal trend by
502 using harmonic model. GSW provides the surface water maps between March and October.

503

504 The SWDF products describe the monthly variation based on the monthly composite data. In fact,
505 quarterly variation can be generated if using quarterly composite data, which have also been provided in the
506 attached Data as well. The area surface water extent in four seasons is estimated as well (Figure 8). The
507 results indicate a general seasonality of dry autumn and wet winter. During the winter of 2017-2018 (Figure
508 8), particularly in January 2018 (Figure 7), France witnessed an intense episode of flooding with several
509 successive flood waves. The highest values of SWDF MOY are related to this long flood period.

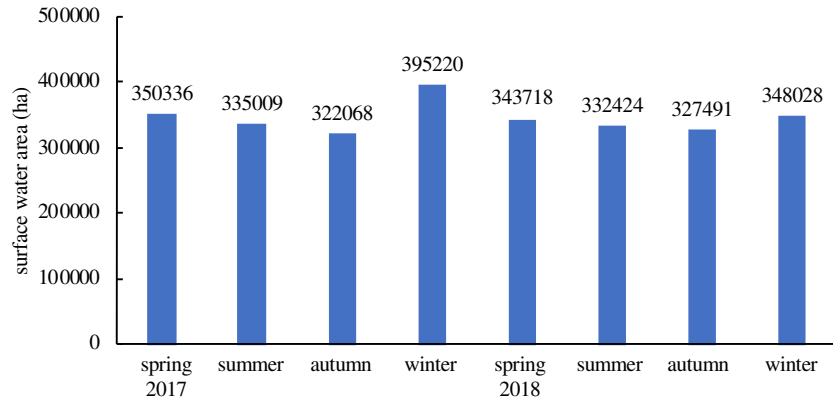
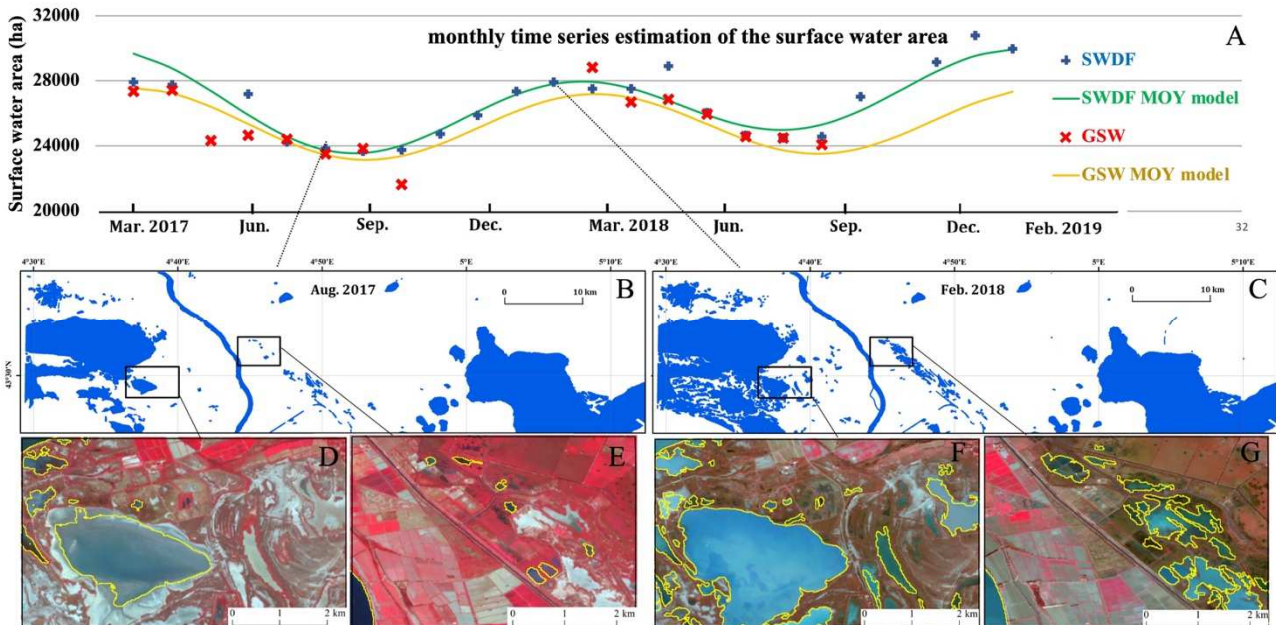


Figure 8. Surface water area of France in four seasons estimated in SWDF product

510

511

512 To illustrate the temporal resolution of SWDF, we focused on a detailed example (Figure 9) of mapped
 513 surface water in the southern coastal areas covering parts of the Camargue Regional Nature Park, the Pond
 514 of Vaccarès, and the lower courses of the Rhône River and the Pond of Berre, which is largest salt water
 515 lake in France, within the department of Bouches-du-Rhône, at the monthly time scale. The MOY surface
 516 water area estimated from SWDF and GSW is also fitted with the sine and cosine functions (Eq. 4). The
 517 result displays dramatic seasonal behavior (Figure 9). In general, the monthly time series trend features the
 518 transition from dry summers beginning as early as June to wet winters beginning in October, which is in
 519 accord with the Mediterranean climate characteristics. In addition, there are only two months (May 2017 and
 520 Nov. 2018) that are extremely affected by clouds in SWDF over the 24 MOYs. The detailed monthly
 521 changes and corresponding false color composite images are provided in Figure S1 and Figure S2 (in the
 522 Supplemental materials S.4).



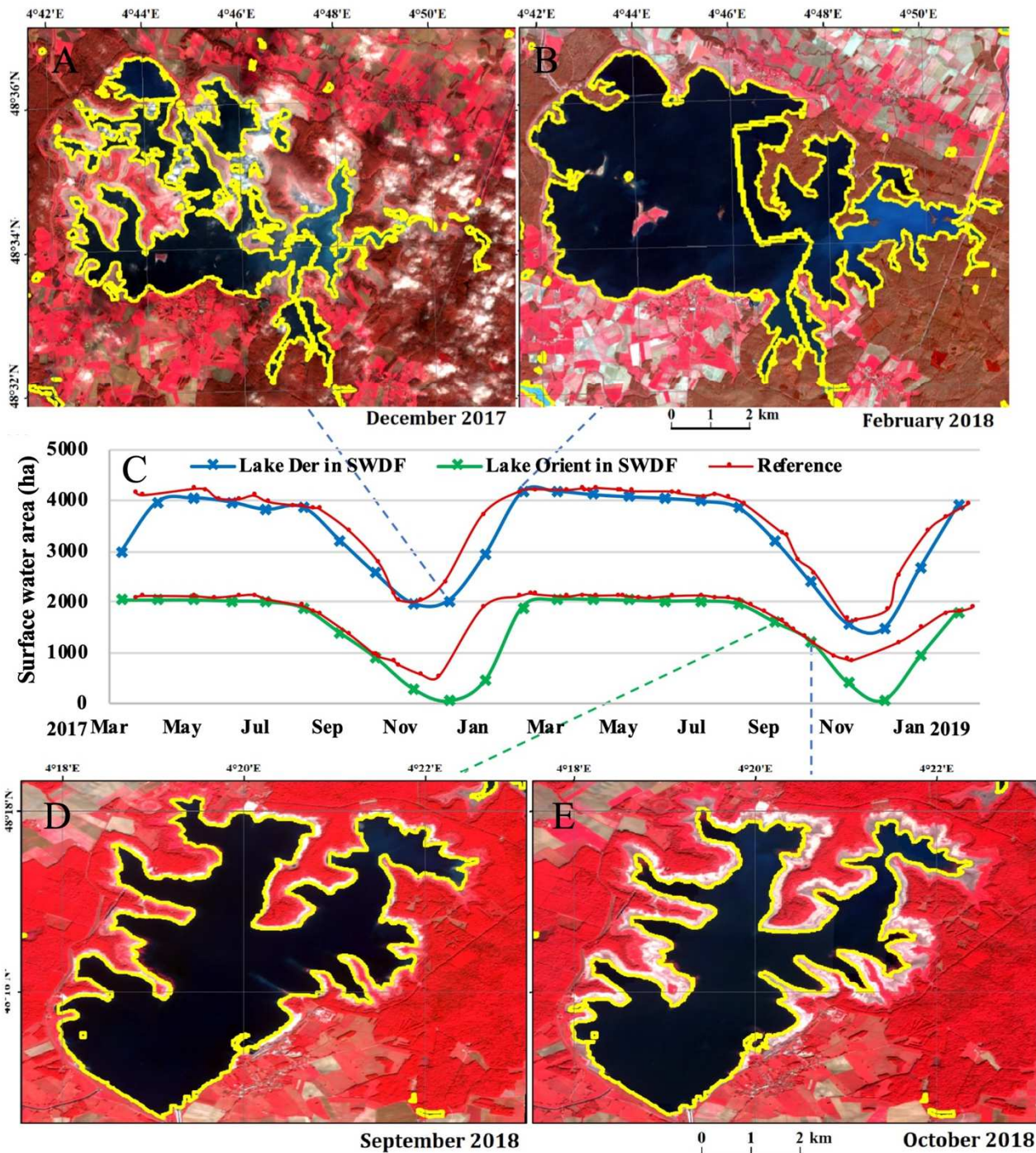
523

524 Figure 9. Monthly time series changes in a part of the southern coastal area. (A) Monthly time series estimation of the
 525 surface water area in the study area SWDF, GSW and fitted models. (B) & (C) are two monthly maps provided by
 526 SWDF. (D-G) display two zoom-in regions, where the surface water extents (yellow lines) overlay the Sentinel-2
 527 monthly composite image.

528 Here, at a more detailed scale, an example of lake dynamics across Lake Der-Chantecoq and Lake
 529 Orient in 2017 and 2018 from the quarterly maps is shown (Figure 10). The surface water extent displays
 530 seasonal variations according to the quarterly time series analysis. Compared to the monthly variation in
 531 Figure 11, the quarterly maps are more robust because clear images are generally available for the whole of
 532 France during the quarterly time span. Nevertheless, the greater accuracy of the spatial distribution reduces
 533 the temporal variation. For example, the changes between December and February (within the period of
 534 winter) and between September and October (within the period of autumn) are noteworthy; yet, the quarterly
 535 map cannot capture these monthly changes. In the monthly product (Figure 11), Lake Der-Chantecoq is
 536 completely filled from December to February, and Lake Orient ran dry during the September and October.
 537 The quarterly product (Figure 10) only displays the dry situation in autumn and the waterlogged state in
 538 winter. The correlation between the SWDF monthly time series products and the reference maps is 0.946 for
 539 Lake Der-Chantecoq and 0.892 for Lake Orient. That is, the monthly map can monitor the variation at
 540 higher temporal resolution with an acceptable extraction accuracy. In addition, the dramatically smallest
 541 surfaces' period occurs between November to February, which cannot be reflected in the GSW product
 542 owing to the data deficiency.



543
 544 Figure 10. Quarterly time series changes in the surface water extent of Lake Der-Chantecoq and Lake
 545 Orient. The yellow lines display the surface water extents provided by SWDF. The background corresponds to the quarterly median
 546 composite data based on Sentinel-2 images.



547

548 Figure 11. Monthly time series changes in Lake Der-Chantecoq and Lake Orient. The curves (C) display the monthly
 549 surface water area estimated by SWDF and the reference values. A, B, D and E are surface water extents (yellow lines)
 550 overlaying on Sentinel-2 images. These monthly variations, including A and B in winter and D and E in autumn,
 551 cannot be reflected by quarterly maps.

552

553 Additionally, 200 sample points are marked as water bodies, non-water bodies and no data by visual
 554 interpretation based on the reference monthly composite images. In total, 4800 sample points over 24
 555 months were obtained with two dimensions ("actual" by manual judgment and "predicted" by the RBSP
 556 method). The overall confusion matrix is presented in Table 7 after excluding 840 no-data sample points
 557 (Table S3 shows the monthly confusion matrix in the Supplemental materials). The ACC and MCC for the

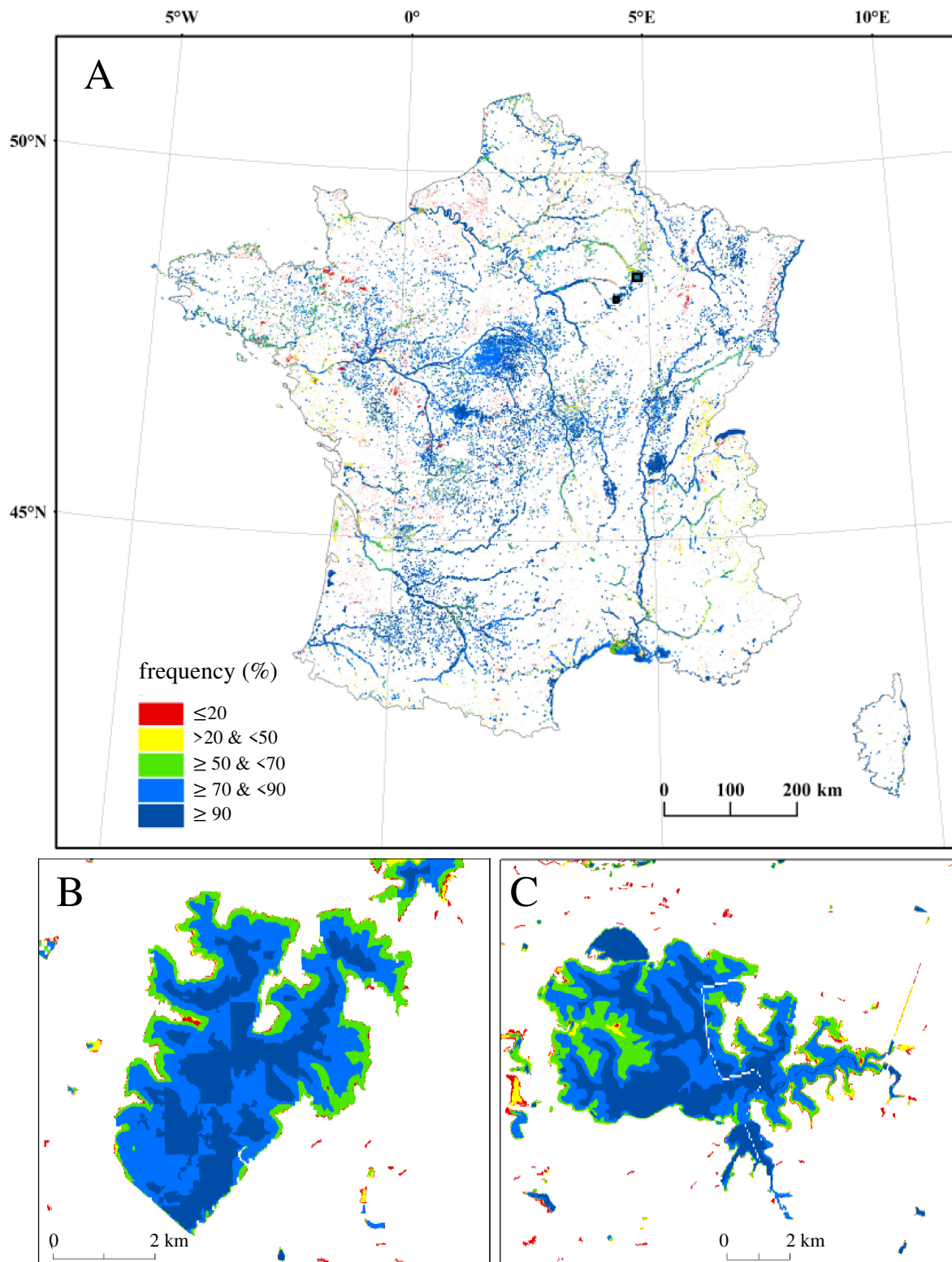
558 general products within a two-year period are 0.932 and 0.865, respectively. Owing to the wet winter season
 559 in November and December, the results during these two months present relatively low accuracy; the ACC
 560 and MCC values are approximately 0.87 and 0.75, respectively.

561 Table 7. Accuracy assessment of sample points

| 840 points: no data available 3960 points: valid MOYs | | Actual reference by visual interpretation | |
|--|-----------|---|-----------|
| | | Water | Non-water |
| Predicted SWDF by the RBSP method | Water | 1589 | 61 |
| | Non-water | 207 | 2103 |
| PA = 0.885; UA = 0.963; ACC = 0.932; MCC = 0.865 | | | |

562 *3.2. Water frequency and annual surface extent*

563 The annual frequency of surface water, expressed as a value from 0 to 100%, reflects the number of
 564 times a pixel is flagged as water over the total number of cloud-free monthly compositions during the year.
 565 Figure 12 displays the annual frequency of surface water in 2018. The satellite-based frequency of water
 566 bodies can be decreased by many factors, including the clouds (omitted by the cloud-screening algorithm),
 567 geometric mismatch and artifacts over certain areas (Zou et al., 2018). In the project, an annual frequency of
 568 no lower than 70% is regarded as a satellite-based permanent water body. Frequencies between 20% and 70%
 569 can be regarded as seasonal water bodies, where have water some time in a year. An annual frequency of no
 570 higher than 20% indicates that the pixels are marked as water bodies during one or two months of the year.
 571 These pixels could be the noise from cloud shadows and inundation zones, which are somewhat mixed in the
 572 annual frequency map and need further consideration.



573
 574 Figure 12. Annual surface water occurrence map in 2018 generated by calculating the frequency of pixels marked as
 575 water bodies in the monthly maps. (A) France, (B) Lake Orient, and (C) Lake Der-Chantecoq. Note: The gap inside the
 576 Lake Der-Chantecoq is from the separate processing of the two divisions (Marne and Haute-Marne).

577 In the project, we generated water body maps in 2017 and 2018 based on the frequency map. The
 578 minimum water extent covering the permanent water bodies was 308,374 ha and 313,808 ha in 2017 and
 579 2018, respectively, while the maximum water extent, including the permanent and seasonal water bodies,

580 was approximately 421,857 ha and 414,449 ha in 2017 and 2018, respectively. Table 8 listed the surface
 581 water area estimated from different HR derived products and the hydrological BD Cartage dataset.

582 Table 8. Surface water area in France estimated from different products

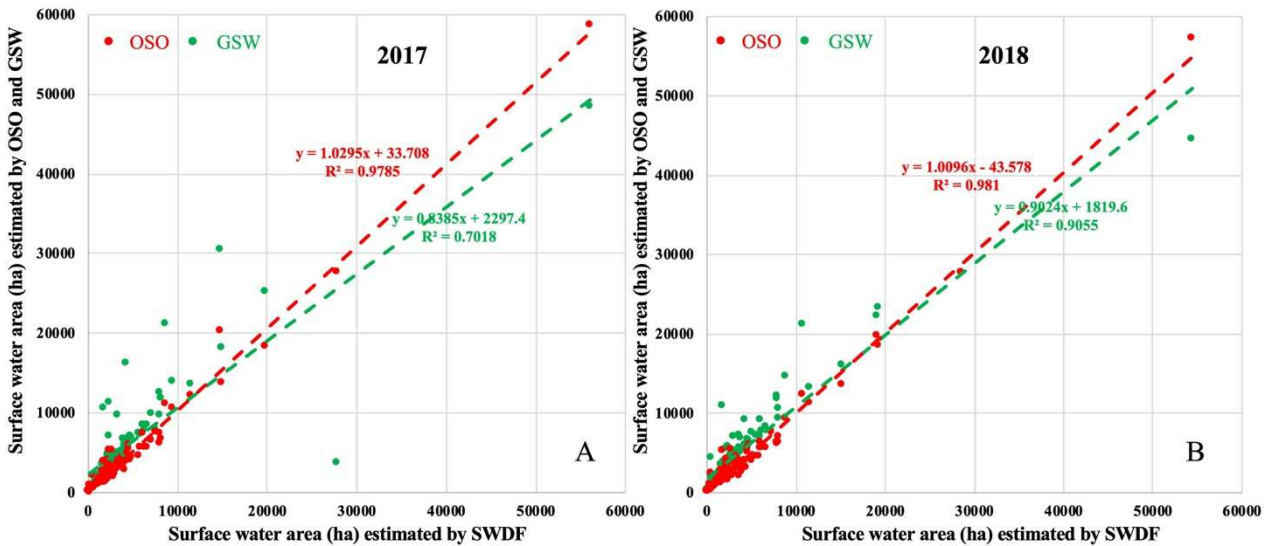
| Surface water area (ha) | SWDF | | GSW | | OSO | BD Cartage in 2016 | |
|-------------------------|-----------|---------|-----------|---------|---------|--------------------|---------|
| | permanent | maximum | permanent | maximum | maximum | permanent | maximum |
| 2017 | 308,374 | 421,857 | 277,959 | 394,297 | 541,912 | 428,401 | 543,319 |
| 2018 | 313,808 | 414,449 | 287,551 | 402,313 | 540,353 | | |

583
 584 These permanent and maximum surface water maps were quantitatively compared with the HR satellite
 585 derived annual maps from 2017 and 2018 (Table 9). The confusion matrix was calculated to determine the
 586 degree of consistency of the surface water extents predicted by the different products. TP and TN denote the
 587 same extracted regions of water bodies and non-water bodies, and FP and FN denote the omission in one
 588 product and commission in another product. Additionally, correlation analysis is performed based on the
 589 surface water areas in 96 administrative divisions. The coefficient of determination (R^2) (Figure 13) of linear
 590 regression is found to be approximately 0.98 for GSW and 0.80 on average for OSO compared with SWDF.
 591 The Pearson correlation coefficient (r) between the SWDF and GSW methods is approximately 0.99 on
 592 average. In general, the SWDF and GSW approaches display a high degree of consistency in both area-
 593 based correlation analysis and region-based confusion matrix aspects, perhaps due to their similar solutions
 594 based on the annual percentage of pixels.

595 Also, the SWDF annual products are evaluated using the BD Carthage hydrological database obtained in
 596 2016. The confusion matrix-based metrics were 0.617 (PA), 0.801 (UA), 0.995 (ACC) and 0.700 (MCC) on
 597 average for the maximum extent and 0.611 (PA), 0.842 (UA), 0.996 (ACC) and 0.715 (MCC) for permanent
 598 water bodies. The relative high UA means that SWDF soundly overcomes the error extraction of water
 599 bodies soundly. That is, the noise is effectively excluded based on the water occurrence analysis. The low
 600 PA means that the SWDF faces greater challenges in detecting the missing parts of the surface water bodies.
 601 However, the hydrological data were obtained before 2016 and thus the dissimilarity cannot be avoided
 602 between the different temporal data.

603 Table 9. Comparison of the annual surface water maximum and permanent extent provided by three satellite derived
 604 products and a hydrological database

| (2017/2018) | | SWDF vs OSO | SWDF vs GSW | OSO vs GSW | SWDF vs BD Cartage |
|----------------|-----|---------------|---------------|---------------|--------------------|
| | r | 0.952 / 0.838 | 0.991 / 0.989 | 0.946 / 0.856 | 0.915 / 0.914 |
| Maximum extent | ACC | 0.996 / 0.995 | 0.997 / 0.997 | 0.995 / 0.994 | 0.995 / 0.995 |
| | MCC | 0.750 / 0.700 | 0.779 / 0.776 | 0.740 / 0.687 | 0.698 / 0.702 |
| Permanent | ACC | Not available | 0.997 / 0.997 | Not available | 0.996 / 0.996 |
| | MCC | Not available | 0.757 / 0.759 | Not available | 0.721 / 0.710 |



605

606

607

Figure 13. Correlation analysis of the annual surface water maximum extent between the SWDF and GSW/OSO methods based on the surface water areas in 96 administrative divisions in (A) 2017 and (B) 2018

608

609

610

611

612

613

614

615

616

617

618

619

620

621

622

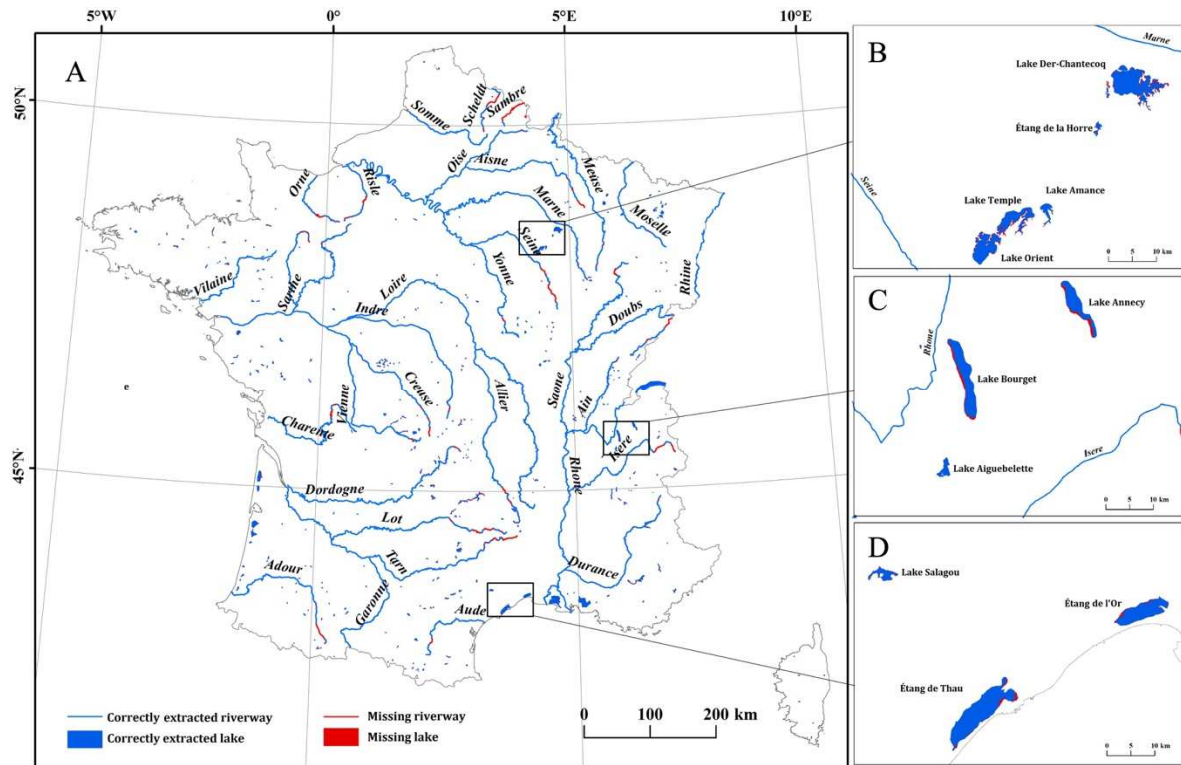
623

624

625

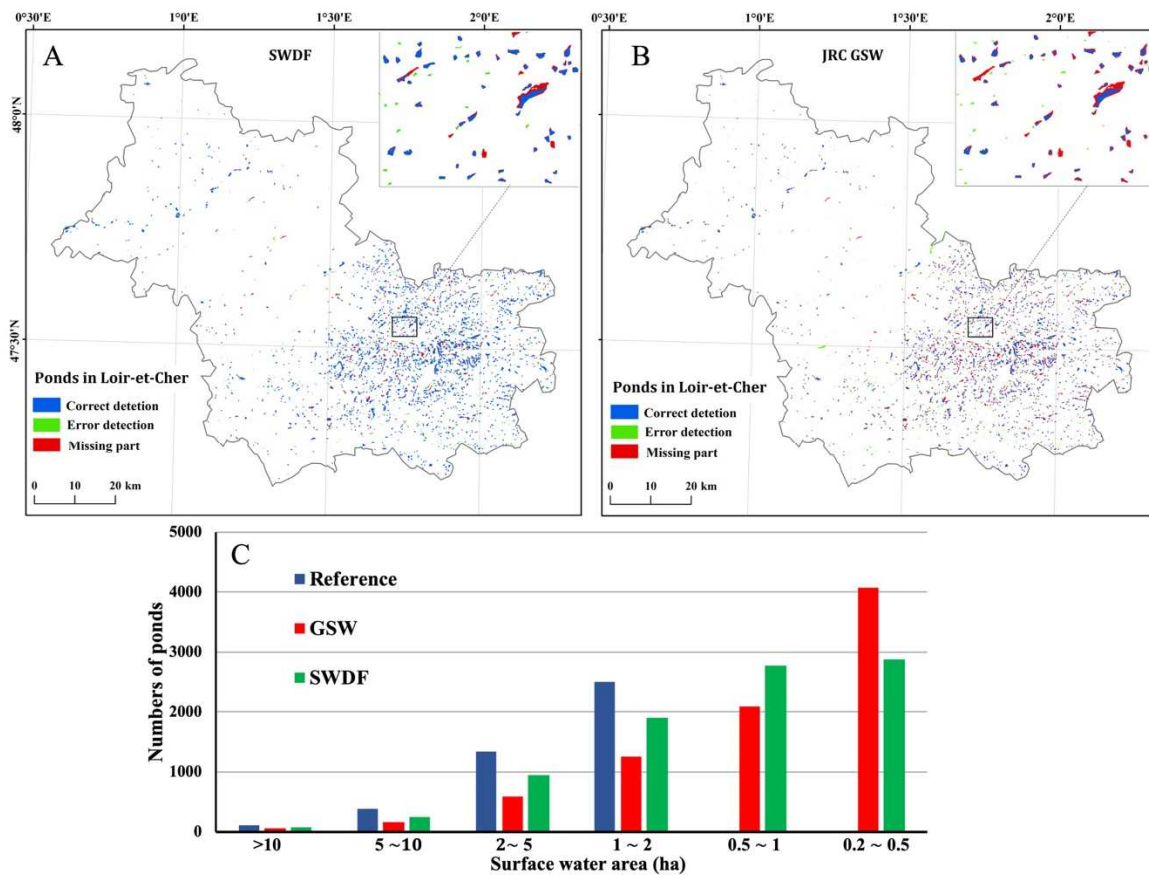
626

Furthermore, the extraction rates (Figure 14) of the main rivers and main lakes are 0.929 and 0.802 in the annual water map of 2018, respectively. Further, the extraction of small water bodies is analyzed based on a large number of ponds spreading across Loir-et-Cher. The confusion matrix analysis of these small water bodies (Figure 15A) indicates that PA, UA, ACC and MCC are 0.683, 0.882, 0.995 and 0.774, respectively. These metrics for the GSW method (Figure 15B) are 0.498, 0.865, 0.993, and 0.653. Both products predict a similar degree of correctness of approximately 90% and commission errors of approximately 10%; however, they face problems with small water bodies related to low completeness and high omission errors. The SWDF method at a 10-m spatial resolution has a higher extraction rate for small water bodies and ponds in Loir-et-Cher than does the GSW method at a 30-m spatial resolution. The reference data include 2498 ponds larger than 1 ha and a total area of 8286 ha (Figure 15C). SWDF detects 1900, 2498 and 2779 ponds larger than 1 ha, 0.6 ha and 0.5 ha, respectively. GSW detects 1265, 2100 and 2498 ponds larger than 1 ha, 0.5 ha and 0.3 ha, respectively. The detailed illustration in Figure 15 indicates that the boundaries of the ponds are subject to extremely omission phenomena (redaa color), especially for GSW, which are mainly caused by the vegetation and vegetation shadows. This kind of omission error reduces the surface water area for each pond. In addition, GSW includes approximately 2000 ponds between 0.2 ha and 0.5 ha, which are generally sparse noise owing to the pixelwise mapping. The official database of the surface water extent faces the problem of the temporal changes, which would reduce its reliability in measuring SWDF dynamic products.



627
628
629
630

Figure 14. Evaluation of the extraction rate of main riverway and lake extents in 2018. (B) (C) and (D) are some zoom-in details in different geological regions of France, which are located in Paris Basin, mountainous Alps and Mediterranean coastal area, respectively.



631
632
633

Figure 15. Evaluation maps of pond extraction in Loir-et-Cher based on the (A) SWDF and (B) GSW products. (C) displays the statistics of the number of ponds in different size.

634

635 **4. Discussion and perspectives**

636 Monthly time series monitoring of surface water bodies at a 10-m resolution was performed for France
637 between March 2017 and February 2019. The SWDF results indicate that Sentinel-2 data can provide higher
638 temporal and spatial resolution information compared with the existing surface water extent products. The
639 proposed RBSP approach tested here allows the frequent updating of the product based on a newly available
640 Sentinel-2 monthly composite image. However, the proposed approach can be further improved to obtain
641 more accurate and complete products, including the commission error of moist soil, the omission error of
642 streams, creeks and frozen water bodies, and the data deficient because of cloud cover.

643 *4.1. Error sources and potential improvements*

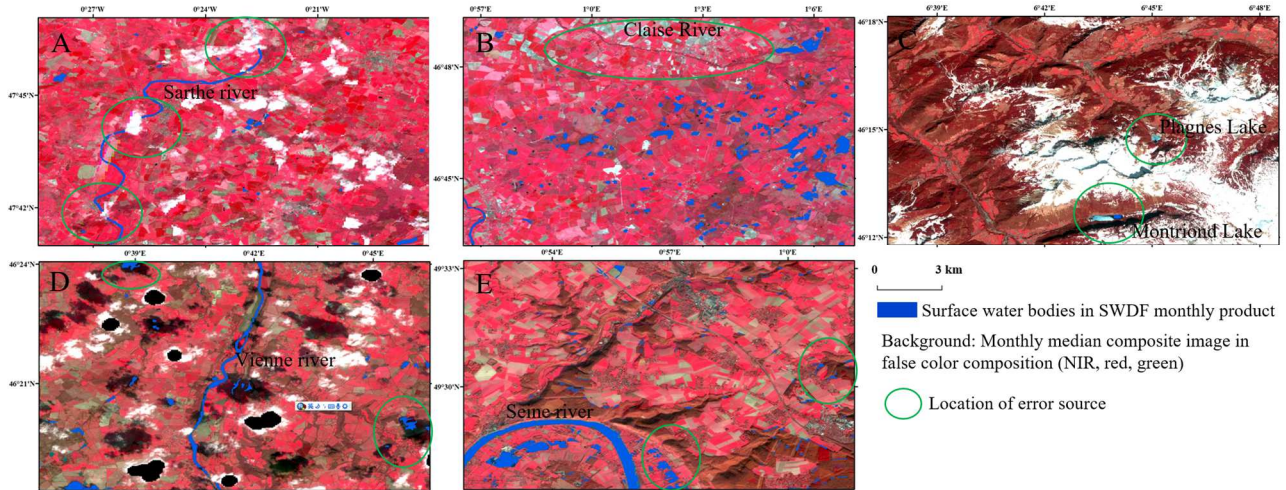
644 Clouds and cloud shadows can cause both the omission error (Figure 16A) and commission errors
645 (Figure 16D), and they reduce the coverage of valid observations, especially during the wet winter in France.
646 In this study, we utilized the Sentinel-2 QA60 band to mask clouds in images with cloud cover percentages
647 of less than 20%. The low cloud cover threshold does not affect the proposed RBSP approach. However, the
648 coverage of the SWDF product could be further improved if an enhanced cloud and cloud shadow algorithm
649 are available and introduced in the preprocessing stage. Recently, the Fmask 4.0 algorithm (Qiu et al., 2019),
650 which robustly detected clouds and cloud shadows in Landsat data, was introduced into Sentinel-2. This
651 enhanced masking algorithm is expected to (i) filter the clear pixels to restrain the commission error and (ii)
652 add experimental data with a loose cloud cover flag to obtain a higher coverage of monthly surface water
653 maps.

654 Wet soil regions distributed in farmland (through irrigation) and wetland areas are somewhat
655 misclassified as surface water bodies based on the rules of spectral indices (Figure 16E). The division of
656 surface water, dry land and wet land is important for monitoring the inner-annual changes in intermittent
657 rivers and ephemeral streams. Thus, some potential ideas involve the synergistically use of Sentinel-1 SAR
658 data (Bousbih et al., 2018) and Landsat 8 thermal information (Sadeghi et al., 2017).

659 RBSP typically faces omission error issues along narrow rivers (Figure 16B) because of 10 meters
660 spatial resolution and the use of superpixel technique, especially when areas are sheltered by vegetation. It is
661 important to restore the completeness of the watercourse in these cases. Potential development steps could
662 be considered to restore rivers from fracture effects by (i) using prior knowledge and GIS data to obtain map
663 layers over time and limit projection distortion, (ii) implementing salient object detection approaches and
664 perceptual organization techniques to address the computational efficiency, and (iii) performing spectral
665 mixture analysis to extract the endmembers of different environments.

666 RBSP regarded ice as the other type of land cover and excluded it from surface water maps in the current
667 project. That is, RBSP would underestimate surface water in winter because the water bodies are frozen
668 (Figure 16C). For the SWDF product, ice is mostly limited to mountainous lakes and hydropower reservoirs

669 in the Alps and Pyrenees areas, which represent a very small percentage of water bodies. The monitoring of
 670 inland river and lake ice indicates significant environment and climate changes (Yang et al., 2020). The
 671 detection of a surface water body can provide the basic layer for further inland ice detection and estimate the
 672 percentages and frequencies of the river and lake ice.



673
 674 Figure 16. Main error sources in the current SWDF products. Omission errors from (A) cloud cover, (B) stream of
 675 Claise River and (C) frozen water bodies in Plagnes Lake and Montriond Lake. Commission errors from (D) cloud
 676 shadow (E) wet land and forests shadow areas.

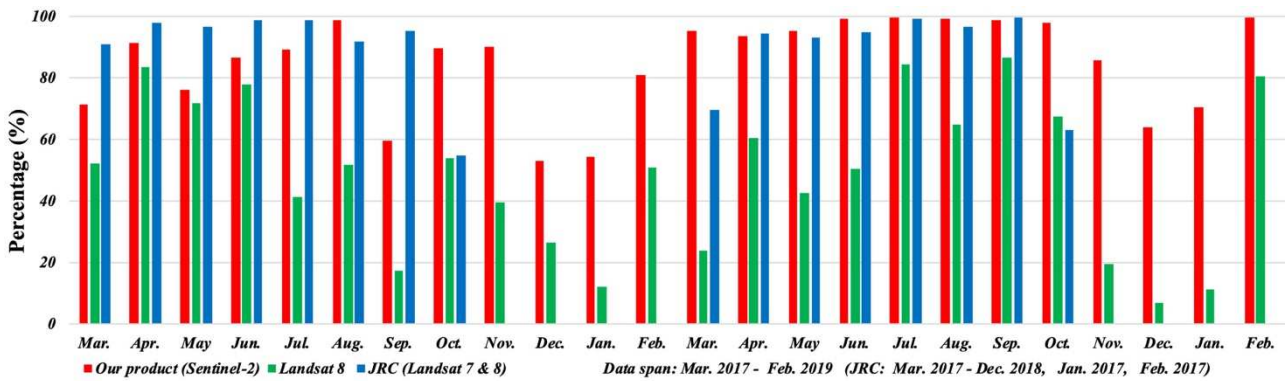
677 In brief, the SWDF method may overestimate the number of water bodies in locations that contain moist
 678 soil and shaded pixels and underestimate the extent of water bodies such as streams, creeks and frozen water
 679 bodies. Commission error exists in the monthly time series maps but can be effectively excluded from the
 680 annual water maps based on frequency calculations. Such accelerated error reduces the accuracy of the
 681 SWDF flood mapping results because bi-temporal maps are applied before and after flooding. Fortunately,
 682 these errors are mainly specific to the monthly maps. The quarterly and annual surface water maps appear to
 683 be more robust than the monthly maps based on the high quality of quarterly composite images and annual
 684 frequency calculations.

685 4.2. Data accessibility and homogeneity of S2 and Landsat

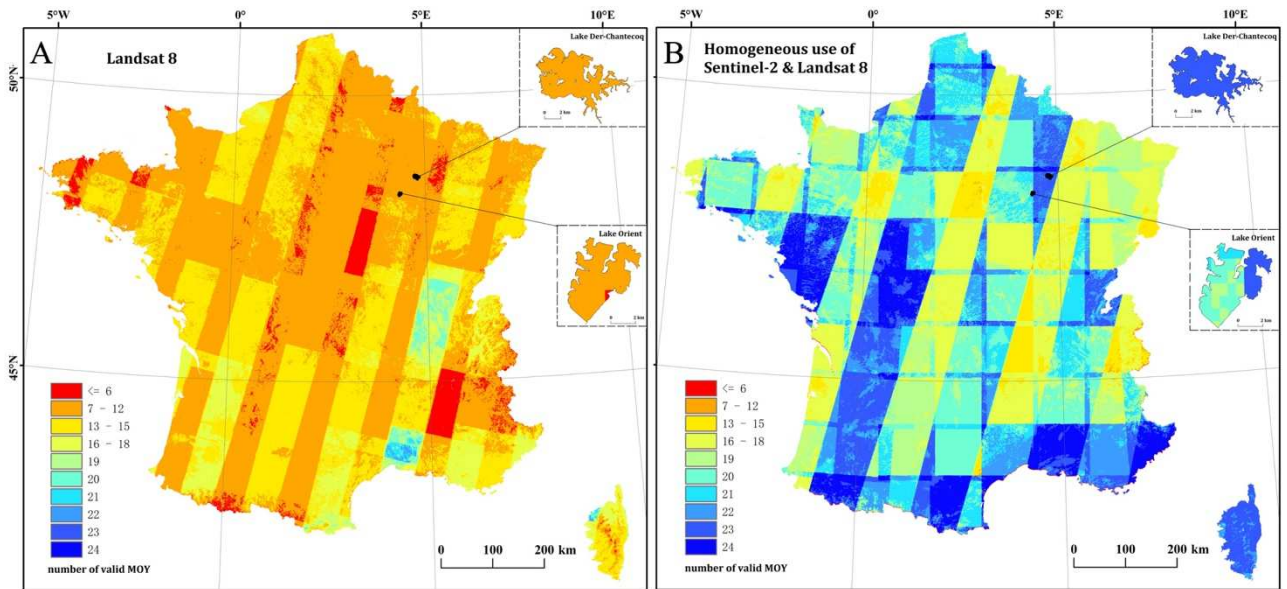
686 To our knowledge, until now, JRC GSW is the only available product that provides the monthly
 687 dynamics of inland surface water bodies. However, GSW could be unavailable in certain months at certain
 688 locations. For France, GSW provides the monthly dynamics between March and October, as shown in
 689 Figure 7.

690 Figure 17 compares the percentage of areas with valid observations in France using Sentinel-2, Landsat
 691 8 and GSW data (synthetic use of Landsat 7 and 8). With a high revisit frequency, Sentinel-2 (85% on
 692 average) can provide more available valid data than Landsat 8 (49% on average) and even GSW (60% on
 693 average). When limited to March through October in the dry season, the available percentage of the area is
 694 similar between the obtained product and the JRC dataset (approximately 90% on average), and the valid
 695 area decreases to 58% on average if only Landsat 8 is utilized. For the quarterly maps, Sentinel-2 provides

696 99.5% coverage, on average, in France, and Landsat 8 covers 85.6% of the entire national area on average.
 697 The SWDF method can provide the complete seasonal dynamic changes in the inland surface water extent,
 698 although the MOY time series analysis requires further improvement to obtain complete coverage, perhaps
 699 by introducing advanced cloud mask algorithms to include more images with
 700 CLOUDY_PIXEL_PERCENTAGE flags or by homogeneously merging Landsat and Sentinel-2 data.
 701 Figure 3 and Figure 18 present the valid MOY maps in a two-year period using Sentinel-2, Landsat 8 and
 702 Sentinel-2 and Landsat 8 combined. Our future work will involve the homogeneous merging of the Landsat
 703 and Sentinel-2 datasets, especially considering the recently published Landsat Analysis-ready Data (ARD)
 704 products and upcoming Landsat 9 scheduled for launch in December 2020.



705
 706 Figure 17. The percentage of the monthly composite data coverage from Sentinel-2, Landsat 8 and the combined use of
 707 Landsat 7 and Landsat 8



708
 709 Figure 18. Number of valid monthly composite images from (A) Landsat 8 and (B) the homogeneous use of Sentinel-2
 710 and Landsat 8 with less than 20% cloud cover

711 5. Conclusion

712 We develop an automated inland surface water detection approach and release a national surface water
 713 dynamics product. To the best of our knowledge, this study is the first to monitor the monthly dynamics of
 714 the surface water extent at a 10-m resolution over a large-scale using Sentinel-2 imagery. The RBSP

715 algorithm runs automatically to delineate surface water bodies in different environments (such as urban
716 scenes, agricultural fields, and mountainous areas). The SWDF product determines the water occurrence in
717 France at monthly time steps and at a 10-m spatial resolution. The geography of France includes coastline
718 areas, mountainous areas, plains, islands and metropolises. Thus, the RBSP approach is intuitively
719 implemented in GEE and has the potential to generate surface water dynamics at other national scopes and
720 even the global scope.

721 The obtained SWDF product is evaluated and validated based on both the HR satellite image derived
722 water maps and official datasets. The annual surface water maps of SWDF show consistency with the
723 publicly released land surface water maps of the JRC GSW, OSO and BD Cartage based on both the spatial
724 distribution and surface area. These products display a high correlation coefficient of over 0.950 for surface
725 water area prediction and high overall accuracies of over 0.995 (ACC) and approximately 0.750 (MCC)
726 based on confusion matrix analysis. Moreover, the MOY SWDF and GSW products exhibit a similar
727 seasonal trend, with a correlation coefficient of 0.940. The SWDF results cover all 24 months in the two-
728 year period, but the GSW method excludes results for the winter seasons from November to February.
729 Additionally, the SWDF method has a higher extraction rate than the GSW method for small water bodies
730 due to its higher spatial resolution of 10 m. For example, the completeness of pond extractions in Loir-et-
731 Cher is 0.683 (SWDF) and 0.498 (GSW) using the two methods, respectively. Moreover, the randomly
732 sampled points show that the monthly water dynamics of SWDF have overall accuracies of 0.932 (ACC)
733 and 0.865 (MCC). The detailed monitoring analysis of Lake Der-Chantecoq and Lake Orient indicates the
734 superiority of MOY compared with conventional seasonal analysis on subtle variation monitoring.

735 Our ongoing work is dedicated to improving the RBSP approach and the general application of the
736 SWDF product. The automatic RBSP approach overestimates the SWDF in wet soil and shadow areas and
737 underestimates the areas of water bodies such as rivers, streams and frozen water bodies. An advanced cloud
738 masking algorithm and soil moisture estimation method could be implemented to reduce the commission
739 error. A salient edge detection approach will be considered to address the omission of river fractures. The
740 monitoring of percentage and frequency of river and lake ice is an interesting topic to be explored in our
741 ongoing work.

742 Overall, the SWDF results provide a unique opportunity for the monthly continuous mapping of the
743 surface water extent at a 10-m scale using time series of composite images. Such monthly continuous time
744 series of surface water dynamics benefit in-depth research on the inner-annual spatiotemporal variability in
745 surface water changes, such as for ephemeral stream and lake monitoring, seasonal variation assessment and
746 inundation mapping. Currently, SWDF has a valid coverage of 85% for the monthly maps and 99.5% for the
747 quarterly maps on average. The valid coverage can be further improved if an enhance cloud and cloud
748 shadow detection algorithm is introduced and a high cloud cover flag is used. Additionally, the
749 homogeneous use of Sentinel-2 and Landsat 8 could further increase the valid coverage of the SWDF
750 product.

751 **SWDF product access**

752 <https://data.mendeley.com/datasets/475kmt7ysv/draft?a=eea5b126-937b-4ccd-ab96-92bcc3c6d637>

753

754 **Acknowledgments**

755 This work is funded by National Key R&D Program Funding (2017YFB0503905-05). The work of X.
756 Yang was supported by the China Scholarship Council (No. 201504490008). We thank the European
757 Commission's Joint Research Centre, Theia, the European Environment Agency, and Système
758 d'Information sur l'Eau (SIE) for providing the reference maps used to validate our products. The Lake de
759 Der and Lake d Orient monitoring was realized within the framework of the SWOT Project.

760 **References**

- 761 Achanta, R., Shaji, A., Smith, K., Lucchi, A., Fua, P., Süsstrunk, S., 2012. SLIC superpixels compared to
762 state-of-the-art superpixel methods. *IEEE Trans. Pattern Anal. Mach. Intell.*
763 doi:10.1109/TPAMI.2012.120
- 764 Achanta, R., Süsstrunk, S., 2017. Superpixels and polygons using simple non-iterative clustering. *Proc. -*
765 *30th IEEE Conf. Comput. Vis. Pattern Recognition, CVPR 2017* 2017-Janua, 4895–4904.
766 doi:10.1109/CVPR.2017.520
- 767 Acharya, T.D., Lee, D.H., Yang, I.T., Lee, J.K., 2016. Identification of water bodies in a landsat 8 OLI
768 image using a J48 decision tree. *Sensors (Switzerland)* 16, 1–16. doi:10.3390/s16071075
- 769 Aires, F., Prigent, C., Fluet-Chouinard, E., Yamazaki, D., Papa, F., Lehner, B., 2018. Comparison of visible
770 and multi-satellite global inundation datasets at high-spatial resolution. *Remote Sens. Environ.* 216,
771 427–441. doi:10.1016/j.rse.2018.06.015
- 772 Allen, G.H., Pavelsky, T., 2018. Global extent of rivers and streams. *Science (80-.)*. 361, 585–588.
773 doi:10.1126/science.aat063
- 774 Arvor, D., Daher, F.R.G., Briand, D., Dufour, S., Rollet, A.J., Simões, M., Ferraz, R.P.D., 2018. Monitoring
775 thirty years of small water reservoirs proliferation in the southern Brazilian Amazon with Landsat time
776 series. *ISPRS J. Photogramm. Remote Sens.* 145, 225–237. doi:10.1016/j.isprsjprs.2018.03.015
- 777 Avisse, N., Tilmant, A., François Müller, M., Zhang, H., 2017. Monitoring small reservoirs' storage with
778 satellite remote sensing in inaccessible areas. *Hydrol. Earth Syst. Sci.* 21, 6445–6459.
779 doi:10.5194/hess-21-6445-2017
- 780 Bartout, P., Touchart, L., 2013. L'inventaire des plans d'eau français: Outil d'une meilleure gestion des eaux
781 de surface. *Ann. Geogr.* 123, 266–289.
- 782 Bayram, B., 2013. An Integrated Approach to Temporal Monitoring of the Shoreline and Basin of Terkos
783 Lake. *J. Coast. Res.* 29, 1427. doi:10.2112/jcoastres-d-12-00084.1
- 784 Bernstein, L.S., 2012. Quick atmospheric correction code: algorithm description and recent upgrades. *Opt.*

785 Eng. 51, 111719. doi:10.1117/1.OE.51.11.111719

786 Bousbih, S., Zribi, M., Hajj, M. El, Baghdadi, N., Lili-Chabaane, Z., Gao, Q., Fanise, P., 2018. Soil moisture
787 and irrigation mapping in a semi-arid region, based on the synergetic use of Sentinel-1 and Sentinel-2
788 data. *Remote Sens.* 10, 1–22. doi:10.3390/rs10121953

789 Campos, J.C., Sillero, N., Brito, J.C., 2012. Normalized difference water indexes have dissimilar
790 performances in detecting seasonal and permanent water in the Sahara-Sahel transition zone. *J. Hydrol.*
791 464–465, 438–446. doi:10.1016/j.jhydrol.2012.07.042

792 Carroll, M.L., Loboda, T. V., 2017. Multi-decadal surface water dynamics in North American tundra.
793 *Remote Sens.* 9, 1–15. doi:10.3390/rs9050497

794 Che, X., Feng, M., Yang, Y., Xiao, T., Huang, S., Xiang, Y., Chen, Z., 2017. Mapping extent dynamics of
795 small lakes using downscaling MODIS surface reflectance. *Remote Sens.* 9. doi:10.3390/rs9010082

796 Chen, F., Zhang, M., Tian, B., Li, Z., 2017. Extraction of Glacial Lake Outlines in Tibet Plateau Using
797 Landsat 8 Imagery and Google Earth Engine. *IEEE J. Sel. Top. Appl. Earth Obs. Remote Sens.* 10,
798 4002–4009. doi:10.1109/JSTARS.2017.2705718

799 Chignell, S.M., Anderson, R.S., Evangelista, P.H., Laituri, M.J., Merritt, D.M., 2015. Multi-temporal
800 independent component analysis and landsat 8 for delineating maximum extent of the 2013 Colorado
801 front range flood. *Remote Sens.* 7, 9822–9843. doi:10.3390/rs70809822

802 Cian, F., Marconcini, M., Ceccato, P., 2018. Normalized Difference Flood Index for rapid flood mapping:
803 Taking advantage of EO big data. *Remote Sens. Environ.* 209, 712–730. doi:10.1016/j.rse.2018.03.006

804 Crétaux, J.F., Abarca-del-Río, R., Bergé-Nguyen, M., Arsen, A., Drolon, V., Clos, G., Maisongrande, P.,
805 2016. Lake Volume Monitoring from Space. *Surv. Geophys.* 37, 269–305. doi:10.1007/s10712-016-
806 9362-6

807 Crist, E.P., 1985. A TM Tasseled Cap equivalent transformation for reflectance factor data. *Remote Sens.*
808 *Environ.* 17, 301–306. doi:10.1016/0034-4257(85)90102-6

809 Csillik, O., 2017. Fast segmentation and classification of very high resolution remote sensing data using
810 SLIC superpixels. *Remote Sens.* 9. doi:10.3390/rs9030243

811 Deng, Y., Jiang, W., Tang, Z., Li, J., Lv, J., Chen, Z., Jia, K., 2017. Spatio-temporal change of lake water
812 extent in Wuhan urban agglomeration based on Landsat images from 1987 to 2015. *Remote Sens.* 9.
813 doi:10.3390/rs9030270

814 Donchyts, G., Schellekens, J., Winsemius, H., Eisemann, E., van de Giesen, N., 2016a. A 30 m Resolution
815 Surface Water Mask Including Estimation of Positional and Thematic Differences Using Landsat 8,
816 SRTM and OpenStreetMap: A Case Study in the Murray-Darling Basin, Australia. *Remote Sens.* 8,
817 386. doi:10.3390/rs8050386

818 Donchyts, G., Winsemius, H., Schellekens, J., Erickson, T., Gao, H., Savenije, H., van de Giesen, N., 2016b.
819 Global 30m Height Above the Nearest Drainage, in: European Geosciences Union.
820 doi:10.13140/RG.2.1.3956.8880

821 Dong, J., Xiao, X., Menarguez, M.A., Zhang, G., Qin, Y., Thau, D., Biradar, C., Moore, B., 2016. Mapping

822 paddy rice planting area in northeastern Asia with Landsat 8 images, phenology-based algorithm and
823 Google Earth Engine. *Remote Sens. Environ.* 185, 142–154. doi:10.1016/j.rse.2016.02.016

824 Dronova, I., Gong, P., Wang, L., 2011. Object-based analysis and change detection of major wetland cover
825 types and their classification uncertainty during the low water period at Poyang Lake, China. *Remote*
826 *Sens. Environ.* 115, 3220–3236. doi:10.1016/j.rse.2011.07.006

827 Drusch, M., Del Bello, U., Carlier, S., Colin, O., Fernandez, V., Gascon, F., Hoersch, B., Isola, C., Laberinti,
828 P., Martimort, P., Meygret, A., Spoto, F., Sy, O., Marchese, F., Bargellini, P., 2012. Sentinel-2: ESA’s
829 Optical High-Resolution Mission for GMES Operational Services. *Remote Sens. Environ.* 120, 25–36.
830 doi:10.1016/j.rse.2011.11.026

831 Du, Y., Zhang, Y., Ling, F., Wang, Q., Li, W., Li, X., 2016. Water bodies’ mapping from Sentinel-2
832 imagery with Modified Normalized Difference Water Index at 10-m spatial resolution produced by
833 sharpening the swir band. *Remote Sens.* 8, 354. doi:10.3390/rs8040354

834 Fan, Y., Chen, S., Zhao, B., Pan, S., Jiang, C., Ji, H., 2018. Shoreline dynamics of the active Yellow River
835 delta since the implementation of Water-Sediment Regulation Scheme: A remote-sensing and
836 statistics-based approach. *Estuar. Coast. Shelf Sci.* 200, 406–419. doi:10.1016/j.ecss.2017.11.035

837 Feng, M., Sexton, J.O., Channan, S., Townshend, J.R., 2016. A global, high-resolution (30-m) inland water
838 body dataset for 2000: first results of a topographic–spectral classification algorithm. *Int. J. Digit.*
839 *Earth* 9, 113–133. doi:10.1080/17538947.2015.1026420

840 Fernández, I., Aguilar, F.J., Aguilar, M.A., Álvarez, M.F., 2014. Influence of data source and training size
841 on impervious surface areas classification using VHR satellite and aerial imagery through an object-
842 based approach. *IEEE J. Sel. Top. Appl. Earth Obs. Remote Sens.* 7, 4681–4691.
843 doi:10.1109/JSTARS.2014.2327159

844 Feyisa, G.L., Meilby, H., Fensholt, R., Proud, S.R., 2014. Automated Water Extraction Index: A new
845 technique for surface water mapping using Landsat imagery. *Remote Sens. Environ.* 140, 23–35.
846 doi:10.1016/j.rse.2013.08.029

847 Fisher, A., Flood, N., Danaher, T., 2016. Comparing Landsat water index methods for automated water
848 classification in eastern Australia. *Remote Sens. Environ.* 175, 167–182. doi:10.1016/j.rse.2015.12.055

849 Ford, M., 2013. Shoreline changes interpreted from multi-temporal aerial photographs and high resolution
850 satellite images: Wotje Atoll, Marshall Islands. *Remote Sens. Environ.* 135, 130–140.
851 doi:10.1016/j.rse.2013.03.027

852 Fort, M., André, M.-F., 2013. *Landscapes and Landforms of France (World Geomorphological Landscapes)*.
853 Springer.

854 Gao, B.-C., 1996. NDWI A Normalized Difference Water Index for Remote Sensing of Vegetation Liquid
855 Water From Space. *Remote Sens. Env.* 7212, 257–266.

856 Gharibbafghi, Z., Tian, J., Reinartz, P., 2018. Modified Superpixel Segmentation for Digital Surface Model
857 Refinement and Building Extraction from Satellite Stereo Imagery. *Remote Sens.* 10, 1824.
858 doi:10.3390/rs10111824

- 859 Ghosh, M.K., Kumar, L., Roy, C., 2015. Monitoring the coastline change of Hatiya Island in Bangladesh
860 using remote sensing techniques. *ISPRS J. Photogramm. Remote Sens.* 101, 137–144.
861 doi:10.1016/j.isprsjprs.2014.12.009
- 862 Gong, M., Zhan, T., Zhang, P., Miao, Q., 2017. Superpixel-Based Difference Representation Learning for
863 Change Detection in Multispectral Remote Sensing Images 55, 2658–2673. doi:10.4018/978-1-5225-
864 5589-6.ch001
- 865 Gong, P., Liu, H., Zhang, M., Li, C., Wang, J., Huang, H., Clinton, N., Ji, L., Li, Wenyu, Bai, Y., Chen, B.,
866 Xu, B., Zhu, Z., Yuan, C., Ping Suen, H., Guo, J., Xu, N., Li, Weijia, Zhao, Y., Yang, J., Yu, C., Wang,
867 X., Fu, H., Yu, L., Dronova, I., Hui, F., Cheng, X., Shi, X., Xiao, F., Liu, Q., Song, L., 2019. Stable
868 classification with limited sample: transferring a 30-m resolution sample set collected in 2015 to
869 mapping 10-m resolution global land cover in 2017. *Sci. Bull.* 2017–2020.
870 doi:10.1016/j.scib.2019.03.002
- 871 Gorelick, N., Hancher, M., Dixon, M., Ilyushchenko, S., Thau, D., Moore, R., 2017. Google Earth Engine:
872 Planetary-scale geospatial analysis for everyone. *Remote Sens. Environ.* 202, 18–27.
873 doi:10.1016/j.rse.2017.06.031
- 874 Hansen, M.C.C., Potapov, P. V, Moore, R., Hancher, M., Turubanova, S.A. a, Tyukavina, A., Thau, D.,
875 Stehman, S.V. V, Goetz, S.J.J., Loveland, T.R.R., Kommareddy, A., Egorov, A., Chini, L., Justice,
876 C.O.O., Townshend, J.R.G.R.G., Patapov, P.V., Moore, R., Hancher, M., Turubanova, S.A. a,
877 Tyukavina, A., Thau, D., Stehman, S.V. V, Goetz, S.J.J., Loveland, T.R.R., Kommareddy, A., Egorov,
878 A., Chini, L., Justice, C.O.O., Townshend, J.R.G.R.G., 2013. High-Resolution Global Maps of 21st
879 century forest cover change. *Science (80-.)*. 342, 850–854. doi:10.1126/science.1244693
- 880 Huang, H., Chen, Y., Clinton, N., Wang, J., Wang, X., Liu, C., Gong, P., Yang, J., Bai, Y., Zheng, Y., Zhu,
881 Z., 2017. Mapping major land cover dynamics in Beijing using all Landsat images in Google Earth
882 Engine. *Remote Sens. Environ.* 202, 166–176. doi:10.1016/j.rse.2017.02.021
- 883 Huang, X., Xie, C., Fang, X., Zhang, L., 2015. Combining Pixel-and Object-Based Machine Learning for
884 Identification of Water-Body Types from Urban High-Resolution Remote-Sensing Imagery. *IEEE J.*
885 *Sel. Top. Appl. Earth Obs. Remote Sens.* 8, 2097–2110. doi:10.1109/JSTARS.2015.2420713
- 886 Huber, C., Battiston, S., Yesou, H., Tinel, C., Laurens, A., Studer, M., 2013. Synergy of VHR pleiades data
887 and SWIR spectral bands for flood detection and impact assessment in urban areas: Case of Krymsk,
888 Russian Federation, in July 2012. *Int. Geosci. Remote Sens. Symp.* 4538–4541.
889 doi:10.1109/IGARSS.2013.6723845
- 890 Huber, C., Li, F., Lai, X., Haouet, S., Durand, A., Butler, S., Burnham, J., Tinel, C., Yizhen, L., Qin, H.,
891 Yésou, H., 2015. Using Pléiades data to understand and monitor a dynamic socio-ecological system:
892 China’s Poyang Lake. *Rev. Fr. Photogramm. Teledetect.* 125–132.
- 893 Hui, F., Xu, B., 2008. International Journal of Remote Modelling spatial - temporal change of Poyang Lake
894 using multitemporal Landsat imagery. *Int. J. Remote Sens.* 29, 5767–5784.
- 895 Inglada, J., Vincent, A., Arias, M., Tardy, B., Morin, D., Rodes, I., 2017. Operational High Resolution Land

896 Cover Map Production at the Country Scale Using Satellite Image Time Series. *Remote Sens.* 9, 95.
897 doi:10.3390/rs9010095

898 Isikdogan, F., Bovik, A.C., Passalacqua, P., 2017. Surface water mapping by deep learning. *IEEE J. Sel. Top.*
899 *Appl. Earth Obs. Remote Sens.* 10, 4909–4918. doi:10.1109/JSTARS.2017.2735443

900 Jakovljević, G., Govedarica, M., Álvarez-Taboada, F., 2018. Waterbody mapping: a comparison of remotely
901 sensed and GIS open data sources. *Int. J. Remote Sens.* 00, 1–29. doi:10.1080/01431161.2018.1538584

902 Klein, I., Dietz, A.J., Gessner, U., Galayeva, A., Myrzakhmetov, A., Kuenzer, C., 2014. Evaluation of
903 seasonal water body extents in Central Asia over the past 27 years derived from medium-resolution
904 remote sensing data. *Int. J. Appl. Earth Obs. Geoinf.* 26, 335–349. doi:10.1016/j.jag.2013.08.004

905 Knoema, 2017. France - Inland water [WWW Document]. URL
906 <https://knoema.com/atlas/France/topics/Land-Use/Area/Inland-water>

907 Kristensen, P., Bogestrand, J., 1996. Surface water quality monitoring. EEA/European Environment Agency,
908 Copenhagen. doi:ISBN: 92-9167-001-4

909 Lasdon, L.S., Waren, A.D., Jain, A., Ratner, M., 1978. Design and Testing of a Generalized Reduced
910 Gradient Code for Nonlinear Programming. *ACM Trans. Math. Softw.* 4, 34–50.
911 doi:10.1145/355769.355773

912 Lee, S.U., Yoon Chung, S., Park, R.H., 1990. A comparative performance study of several global
913 thresholding techniques for segmentation. *Comput. Vision, Graph. Image Process.* 52, 171–190.
914 doi:10.1016/0734-189X(90)90053-X

915 Lehner, B., Döll, P., 2004. Development and validation of a global database of lakes, reservoirs and
916 wetlands. *J. Hydrol.* 296, 1–22. doi:10.1016/j.jhydrol.2004.03.028

917 Li, W., Gong, P., 2016. Continuous monitoring of coastline dynamics in western Florida with a 30-year time
918 series of Landsat imagery. *Remote Sens. Environ.* 179, 196–209. doi:10.1016/j.rse.2016.03.031

919 Li, Y., Gong, X., Guo, Z., Xu, K., Hu, D., Zhou, H., 2016. An index and approach for water extraction using
920 Landsat–OLI data. *Int. J. Remote Sens.* 37, 3611–3635. doi:10.1080/01431161.2016.1201228

921 Liu, Y., Yue, H., 2017. Estimating the fluctuation of Lake Hulun, China, during 1975–2015 from satellite
922 altimetry data. *Environ. Monit. Assess.* 189. doi:10.1007/s10661-017-6346-z

923 Lu, S., Ma, J., Ma, X., Tang, H., Zhao, H., Hasan Ali Baig, M., 2018. Time series of Inland Surface Water
924 Dataset in China (ISWDC) for 2000–2016 derived from MODIS archives. *Earth Syst. Sci.*
925 *Data Discuss.* 1–19. doi:10.5194/essd-2018-134

926 Malahlela, O.E., 2016. Inland waterbody mapping: towards improving discrimination and extraction of
927 inland surface water features. *Int. J. Remote Sens.* 37, 4574–4589.
928 doi:10.1080/01431161.2016.1217441

929 McFeeters, S.K., 1996. The use of the Normalized Difference Water Index (NDWI) in the delineation of
930 open water features. *Int. J. Remote Sens.* 17, 1425–1432. doi:10.1080/01431169608948714

931 Mitkari, K. V., Arora, M.K., Tiwari, R.K., 2017. Extraction of Glacial Lakes in Gangotri Glacier Using
932 Object-Based Image Analysis. *IEEE J. Sel. Top. Appl. Earth Obs. Remote Sens.* 10, 5275–5283.

933 doi:10.1109/JSTARS.2017.2727506

934 Mueller, N., Lewis, A., Roberts, D., Ring, S., Melrose, R., Sixsmith, J., Lymburner, L., McIntyre, A., Tan,
935 P., Curnow, S., Ip, A., 2016. Water observations from space: Mapping surface water from 25 years of
936 Landsat imagery across Australia. *Remote Sens. Environ.* 174, 341–352. doi:10.1016/j.rse.2015.11.003

937 Ogilvie, A., Belaud, G., Massuel, S., Mulligan, M., Le Goulven, P., Calvez, R., 2018a. Surface water
938 monitoring in small water bodies: Potential and limits of multi-sensor Landsat time series. *Hydrol.*
939 *Earth Syst. Sci.* 22, 4349–4380. doi:10.5194/hess-22-4349-2018

940 Ogilvie, A., Belaud, G., Massuel, S., Mulligan, M., Le Goulven, P., Malaterre, P.O., Calvez, R., 2018b.
941 Combining Landsat observations with hydrological modelling for improved surface water monitoring
942 of small lakes. *J. Hydrol.* 566, 109–121. doi:10.1016/j.jhydrol.2018.08.076

943 Ohanya, S.O., Omondi, P.A., Gonçalves, R.M., Forootan, E., Heck, B., Fleming, K., Kusche, J., Kiema,
944 J.B.K., Awange, J.L., 2013. Understanding the decline of water storage across the Ramsar-Lake
945 Naivasha using satellite-based methods. *Adv. Water Resour.* 60, 7–23.
946 doi:10.1016/j.advwatres.2013.07.002

947 Pan, H., Xu, X., Luo, X., Tong, X., Xie, H., 2016. Automated Subpixel Surface Water Mapping from
948 Heterogeneous Urban Environments Using Landsat 8 OLI Imagery. *Remote Sens.* 8, 584.
949 doi:10.3390/rs8070584

950 Pardo-Pascual, J.E., Almonacid-Caballer, J., Ruiz, L.A., Palomar-Vázquez, J., 2012. Automatic extraction of
951 shorelines from Landsat TM and ETM+ multi-temporal images with subpixel precision. *Remote Sens.*
952 *Environ.* 123, 1–11. doi:10.1016/j.rse.2012.02.024

953 Pekel, J.F., Cottam, A., Gorelick, N., Belward, A.S., 2016. High-resolution mapping of global surface water
954 and its long-term changes. *Nature* 540, 418–422. doi:10.1038/nature20584

955 Pekel, J.F., Vancutsem, C., Bastin, L., Clerici, M., Vanbogaert, E., Bartholomé, E., Defourny, P., 2014. A
956 near real-time water surface detection method based on HSV transformation of MODIS multi-Spectral
957 time series data. *Remote Sens. Environ.* 140, 704–716. doi:10.1016/j.rse.2013.10.008

958 Pesaresi, M., Ehrlich, D., Florczyk, A.J., Freire, S., Julea, A., Kemper, T., Soille, P., Syrris, V., 2015. GHS
959 built-up grid, derived from Landsat, multitemporal (1975, 1990, 2000, 2014), European Commission,
960 Joint Research Centre, JRC Data Catalogue. doi:10.2788/656115

961 Qiu, S., Zhu, Z., He, B., 2019. Fmask 4.0: Improved cloud and cloud shadow detection in Landsats 4–8 and
962 Sentinel-2 imagery. *Remote Sens. Environ.* 231, 111205. doi:10.1016/j.rse.2019.05.024

963 Ren, X., Malik, J., 2003. Learning a Classification Model for Segmentation, in: ICCV.
964 doi:10.21313/hawaii/9780824839673.003.0030

965 Rokni, K., Ahmad, A., Selamat, A., Hazini, S., 2014. Water feature extraction and change detection using
966 multitemporal landsat imagery. *Remote Sens.* 6, 4173–4189. doi:10.3390/rs6054173

967 Rover, J., Wylie, B.K., Ji, L., 2010. A self-trained classification technique for producing 30 m percent-water
968 maps from Landsat data. *Int. J. Remote Sens.* 31, 2197–2203. doi:10.1080/01431161003667455

969 Sadeghi, M., Babaeian, E., Tuller, M., Jones, S.B., 2017. The optical trapezoid model: A novel approach to

970 remote sensing of soil moisture applied to Sentinel-2 and Landsat-8 observations. *Remote Sens.*
971 *Environ.* 198, 52–68. doi:10.1016/j.rse.2017.05.041

972 Sagar, S., Roberts, D., Bala, B., Lymburner, L., 2017. Extracting the intertidal extent and topography of the
973 Australian coastline from a 28 year time series of Landsat observations. *Remote Sens. Environ.* 195,
974 153–169. doi:10.1016/j.rse.2017.04.009

975 Sheng, Y., Song, C., Wang, J., Lyons, E.A., Knox, B.R., Cox, J.S., Gao, F., 2016. Representative lake water
976 extent mapping at continental scales using multi-temporal Landsat-8 imagery. *Remote Sens. Environ.*
977 185, 129–141. doi:10.1016/j.rse.2015.12.041

978 Shi, Y., Feng, L., Gong, J., 2017. Four decades of the morphological dynamics of the lakes in the Jiangnan
979 Plain using Landsat observations. *Water Environ. J.* 31, 353–359. doi:10.1111/wej.12250

980 Silveira, A., Saleska, S., Waterloo, M., Rodrigues, G., Cuartas, L.A., Hodnett, M., Rennó, C.D., Nobre, A.D.,
981 2011. Height Above the Nearest Drainage – a hydrologically relevant new terrain model. *J. Hydrol.*
982 404, 13–29. doi:10.1016/j.jhydrol.2011.03.051

983 Sivanpillai, R., Miller, S.N., 2010. Improvements in mapping water bodies using ASTER data. *Ecol. Inform.*
984 5, 73–78. doi:10.1016/j.ecoinf.2009.09.013

985 Stutz, D., Hermans, A., Leibe, B., 2018. Superpixels: An evaluation of the state-of-the-art. *Comput. Vis.*
986 *Image Underst.* 166, 1–27. doi:10.1016/j.cviu.2017.03.007

987 Sun, R., Chen, L., 2012. How can urban water bodies be designed for climate adaptation? *Landsc. Urban*
988 *Plan.* 105, 27–33. doi:10.1016/j.landurbplan.2011.11.018

989 Sun, X., Li, L., Zhang, B., Chen, D., Gao, L., 2015. Soft urban water cover extraction using mixed training
990 samples and Support Vector Machines. *Int. J. Remote Sens.* 36, 3331–3344.
991 doi:10.1080/01431161.2015.1042594

992 Terasmaa, J., Bartout, P., Marzecova, A., Touchart, L., Vandiel, E., Koff, T., Choffel, Q., Kapanen, G.,
993 Maleval, V., Vainu, M., Millot, C., Qsair, Z., Al Domany, M., 2019. A quantitative assessment of the
994 contribution of small standing water bodies to the European waterscapes – case of Estonia and France.
995 *Heliyon* 5. doi:10.1016/j.heliyon.2019.e02482

996 Thomas, R.F., Kingsford, R.T., Lu, Y., Cox, S.J., Sims, N.C., Hunter, S.J., 2015. Mapping inundation in the
997 heterogeneous floodplain wetlands of the Macquarie Marshes, using Landsat Thematic Mapper. *J.*
998 *Hydrol.* 524, 194–213. doi:10.1016/j.jhydrol.2015.02.029

999 Trianni, G., Lisini, G., Angiuli, E., Moreno, E.A., Dondi, P., Gaggia, A., Gamba, P., 2015. Scaling up to
1000 national/regional urban extent mapping using landsat data. *IEEE J. Sel. Top. Appl. Earth Obs. Remote*
1001 *Sens.* 8, 3710–3719. doi:10.1109/JSTARS.2015.2398032

1002 Tseng, K.H., Shum, C.K., Kim, J.W., Wang, X., Zhu, K., Cheng, X., 2016. Integrating Landsat Imageries
1003 and Digital Elevation Models to Infer Water Level Change in Hoover Dam. *IEEE J. Sel. Top. Appl.*
1004 *Earth Obs. Remote Sens.* 9, 1696–1709. doi:10.1109/JSTARS.2015.2500599

1005 Tulbure, M.G., Broich, M., 2013. Spatiotemporal dynamic of surface water bodies using Landsat time-series
1006 data from 1999 to 2011. *ISPRS J. Photogramm. Remote Sens.* 79, 44–52.

1007 doi:10.1016/j.isprsjprs.2013.01.010

1008 Tulbure, M.G., Broich, M., Stehman, S. V., Kommareddy, A., 2016. Surface water extent dynamics from
1009 three decades of seasonally continuous Landsat time series at subcontinental scale in a semi-arid region.
1010 *Remote Sens. Environ.* 178, 142–157. doi:10.1016/j.rse.2016.02.034

1011 Verpoorter, C., Kutser, T., Seekell, D.A., Tranvik, L.J., 2014. A global inventory of lakes based on high-
1012 resolution satellite imagery. *Geophys. Res. Lett.* 41, 6396–6402. doi:10.1002/2014GL060641

1013 Verpoorter, C., Kutser, T., Tranvik, L., 2012. Automated mapping of water bodies using landsat
1014 multispectral data. *Limnol. Oceanogr. Methods* 10, 1037–1050. doi:10.4319/lom.2012.10.1037

1015 Wang, J., Sheng, Y., Tong, T.S.D., 2014. Monitoring decadal lake dynamics across the Yangtze Basin
1016 downstream of Three Gorges Dam. *Remote Sens. Environ.* 152, 251–269.
1017 doi:10.1016/j.rse.2014.06.004

1018 Wang, S., Baig, M.H.A., Zhang, L., Jiang, H., Ji, Y., Zhao, H., Tian, J., 2015. A simple enhanced water
1019 index (EWI) for percent surface water estimation using landsat data. *IEEE J. Sel. Top. Appl. Earth Obs.*
1020 *Remote Sens.* 8, 90–97. doi:10.1109/JSTARS.2014.2387196

1021 Wang, Z., Liu, J., Li, J., Zhang, D.D., 2018. Multi-Spectral Water Index (MuWI): A Native 10-m Multi-
1022 Spectral Water Index for accurate water mapping on sentinel-2. *Remote Sens.* 10, 1–21.
1023 doi:10.3390/rs10101643

1024 Xie, C., Huang, X., Zeng, W., Fang, X., 2016. A novel water index for urban high-resolution eight-band
1025 WorldView-2 imagery. *Int. J. Digit. Earth* 9, 925–941. doi:10.1080/17538947.2016.1170215

1026 Xie, H., Luo, X., Xu, X., Pan, H., Tong, X., 2016. Evaluation of Landsat 8 OLI imagery for unsupervised
1027 inland water extraction. *Int. J. Remote Sens.* 37, 1826–1844. doi:10.1080/01431161.2016.1168948

1028 Xu, H., 2006. Modification of normalised difference water index (NDWI) to enhance open water features in
1029 remotely sensed imagery. *Int. J. Remote Sens.* 27, 3025–3033. doi:10.1080/01431160600589179

1030 Yamazaki, D., Trigg, M.A., Ikeshima, D., 2015. Development of a global ~90m water body map using
1031 multi-temporal Landsat images. *Remote Sens. Environ.* 171, 337–351. doi:10.1016/j.rse.2015.10.014

1032 Yang, X., Chen, L., 2017. Evaluation of automated urban surface water extraction from Sentinel-2A
1033 imagery using different water indices. *J. Appl. Remote Sens.* 11. doi:10.1117/1.JRS.11.026016

1034 Yang, X., Pavelsky, T.M., Allen, G.H., 2020. The past and future of global river ice. *Nature* 577, 69–73.
1035 doi:10.1038/s41586-019-1848-1

1036 Yang, X., Qin, Q., Grussenmeyer, P., Koehl, M., 2018. Urban surface water body detection with suppressed
1037 built-up noise based on water indices from Sentinel-2 MSI imagery. *Remote Sens. Environ.* 219, 259–
1038 270. doi:10.1016/j.rse.2018.09.016

1039 Yang, X., Zhao, S., Qin, X., Zhao, N., Liang, L., 2017. Mapping of urban surface water bodies from
1040 sentinel-2 MSI imagery at 10 m resolution via NDWI-based image sharpening. *Remote Sens.* 9.
1041 doi:10.3390/rs9060596

1042 Yésou, H., Huber, C., Lai, X., Averty, S., Li, J., Daillet, S., Bergé Nguyen, M., Chen, X., Huang, Burnham,
1043 J., Jean-François, C., Tiphany, M., Jinggang, L., Rémi, A., 2011. Nine years of water resources

1044 monitoring over the middle reaches of the Yangtze River, with ENVISAT, MODIS, Beijing-1 time
1045 series, Altimetric data and field measurements. *Lakes Reserv. Res. Manag.* 16, 231–247.
1046 doi:10.1111/j.1440-1770.2011.00481.x

1047 Yésou, H., Pottier, E., Mercier, G., Grizonnet, M., Haouet, S., Giros, A., Faivre, R., Huber, C., Michel, J.,
1048 2016. Synergy of Sentinel-1 and Sentinel-2 imagery for wetland monitoring information extraction
1049 from continuous flow of sentinel images applied to water bodies and vegetation mapping and
1050 monitoring. *Int. Geosci. Remote Sens. Symp.* 2016-Novem, 162–165.
1051 doi:10.1109/IGARSS.2016.7729033

1052 Zhang, G., Jia, X., Hu, J., 2015. Superpixel-based graphical model for remote sensing image mapping. *IEEE*
1053 *Trans. Geosci. Remote Sens.* 53, 5861–5871. doi:10.1109/TGRS.2015.2423688

1054 Zhang, T., Ren, H., Qin, Q., Zhang, C., Sun, Y., 2017. Surface Water Extraction from Landsat 8 OLI
1055 Imagery Using the LBV Transformation. *IEEE J. Sel. Top. Appl. Earth Obs. Remote Sens.* 10, 4417–
1056 4429. doi:10.1109/JSTARS.2017.2719029

1057 Zhang, T., Yang, X., Hu, S., Su, F., 2013. Extraction of coastline in aquaculture coast from multispectral
1058 remote sensing images: Object-based region growing integrating edge detection. *Remote Sens.* 5,
1059 4470–4487. doi:10.3390/rs5094470

1060 Zhou, Y., Luo, J., Shen, Z., Hu, X., Yang, H., 2014. Multiscale water body extraction in urban environments
1061 from satellite images. *IEEE J. Sel. Top. Appl. Earth Obs. Remote Sens.* 7, 4301–4312.
1062 doi:10.1109/JSTARS.2014.2360436

1063 Zhu, Z., Woodcock, C.E., 2014. Continuous change detection and classification of land cover using all
1064 available Landsat data. *Remote Sens. Environ.* 144, 152–171. doi:10.1016/j.rse.2014.01.011

1065 Zhu, Z., Woodcock, C.E., 2012. Object-based cloud and cloud shadow detection in Landsat imagery.
1066 *Remote Sens. Environ.* 118, 83–94. doi:10.1016/j.rse.2011.10.028

1067 Zhu, Z., Woodcock, C.E., Olofsson, P., 2012. Continuous monitoring of forest disturbance using all
1068 available Landsat imagery. *Remote Sens. Environ.* 122, 75–91. doi:10.1016/j.rse.2011.10.030

1069 Zou, Z., Xiao, X., Dong, J., Qin, Y., Doughty, R.B., Menarguez, M.A., Zhang, G., Wang, J., 2018.
1070 Divergent trends of open-surface water body area in the contiguous United States from 1984 to 2016.
1071 *Proc. Natl. Acad. Sci. U. S. A.* 115, 3810–3815. doi:10.1073/pnas.1719275115

1072 Zou, Z., Xiao, X., Menarguez, M.A., Dong, J., Hooker, K. V., Doughty, R.B., Qin, Y., David Hambright, K.,
1073 2017. Continued decrease of open surface water body area in Oklahoma during 1984–2015. *Sci. Total*
1074 *Environ.* 595, 451–460. doi:10.1016/j.scitotenv.2017.03.259

1075